Stealth and bright fluorescent polymeric nanoparticles coated with pluronic: stability and live tracking in mouse brain

Igor Khalin,[1,§] Doriane Heimburger,[2,§] Nina Melnychuk,[2] Mayeul Collot,[2] Bernhard Groschup[1], Farida Hellal[1,3], Andreas Reisch,[2,*] Nikolaus Plesnila,[1,3,*] Andrey S. Klymchenko[2,*]

1. Institute for Stroke and Dementia Research (ISD), Klinikum der Universität München, Feodor-Lynen-Straße 17, D-81377 Munich

2. Laboratoire de Bioimagerie et Pathologies, UMR 7021 CNRS, Université de Strasbourg, Faculte de Pharmacie, 74, Route du Rhin, 67401 Illkirch, France

3. Cluster for Systems Neurology (SyNergy), Munich, Germany

[§] These authors contributed equally to this work.

*Corresponding authors: andrey.klymchenko@unistra.fr, reisch@unistra.fr, and nikolaus.plesnila@med.uni-muenchen.de

Abstract

The inability to visualize single organic nanoparticles (NPs) *in vivo* is an unsolved issue in the field of nanomedicine. To enable high single particle fluorescence, we loaded polymer poly(methyl methacrylate)-sulfonate (PMMA-SO_3H) NPs with octadecyl rhodamine B together with hydrophobic counter-ions as a fluorophore insulator to prevent aggregation-induced quenching. To create NPs with stealth properties we used the amphiphilic block copolymers pluronic F-127 and F-68.

Fluorescence correlation spectroscopy (FCS) and Förster resonance energy transfer (FRET) showed that pluronics remain at the NP surface after dialysis (density: one amphiphile per 5.5 nm^2) and protected NPs from degradation by serum proteins and surfactants. Single particle brightness was increased 150-fold as compared to commercially available preparations by increasing dye loading to 20 wt% and optimizing particle size. Added to primary cultured neurons, these NPs were stable and interacted with dendrites and axons. After intravenous injection in mice, NPs could be tracked in cerebral vessels for at least 1h by *in vivo* two-photon microscopy. Following brain injury or neuroinflammation, NPs extravasated from meningeal vessels, were taken up by meningeal macrophages, and entered the brain parenchyma.

In summary, we developed biocompatible NPs suitable for drug delivery with *in vitro* and *in vivo* stealth properties and extremely bright fluorescence. Thus, individual NPs could be tracked in mouse brain and their dynamics visualized with subcellular resolution. Using superbright NPs may thus open new avenues for the investigation of NPs in living organisms.

Introduction

Nanoparticles (NPs) have been proposed as "magic bullets", capable to eliminate specifically and selectively pathogens or tumors, notably through targeted and controlled delivery of active compounds.[1,2] However, the last decade has revealed a different picture in view of surprisingly low percentage of nanoparticles actually reaching the target site and the potential toxicity of nanomaterials.[3–5] The typical bottlenecks related to this problem are rapid clearance from systemic circulation, difficulties for NPs to escape the reticuloendothelial system (RES) and to pass barriers between physiological compartments, e.g. the skin, the endothelium, or the blood-brain-barrier. On the other hand, nanoparticles have gained importance as contrast agents in, e.g., MRI,[6] PET-scan,[7] X-ray,[8] medical ultrasound,[9] and fluorescence biomedical imaging.[10] These techniques help can help to better understand and overcome the current limitations of NPs for drug delivery. In particular, following NPs at the single particle level in vivo could be of great help in this endeavor.[11,12]

Particularly, in neuro-nanomedicine, the blood-brain barrier (BBB) remains very challenging for NPs to cross and therefore their bio-distribution in the brain is a particularly important topic in this field.[13] Obviously, the lack of direct methods of NPs' observation is making rigor to establish a good brain targeting, therefore detection at the single-particle level with good spatial-temporal resolution could be a key solution for the future development of CNS drug-delivery systems. It was already reported the possibility of single-particle tracking in zebrafish using counterion-enhanced dye loaded lipid-nanodroplets,[14] however the tracking of single NPs *in vivo* in the brain of rodents was not demonstrated so far.

Meaningful monitoring of the behavior of single NPs in vivo requires the ability to image NPs with sufficient spatial and temporal resolution. Even though many NPs have been reported as magnetic resonance imaging (MRI) contrast agents, the achievable resolution is by far too low for imaging at the single particle level.[15] Probably the best technique to achieve such a resolution is fluorescence imaging thank to recent improvements in optical microscopy down to single-molecule sensitivity.[11,16–18] However, in this case very high brightness of the probe is required. In the field of organic nanomaterials, fluorescent polymer NPs as conjugated polymer particles and dye-loaded polymer NPs have emerged over the last years as very bright fluorescent labels.[19–21] This was made possible by the development of different approaches to overcome aggregation-caused quenching of the dyes encapsulated at high concentrations within the NPs, e.g. aggregation-induced emission dyes [22,23] or the use of bulky counterions.[21,24]

A particularly bright fluorescent polymer NP system is based on poly(methyl methacrylate) (PMMA) NPs loaded with the salt of a rodamine B derivative (R18) and a highly fluorinated tetraphenylborate (F5-TPB) as bulky counterion.[25–28] PMMA is known to be a fully biocompatible polymer and has already had a long history in medical applications.[29] Dye-loaded NPs based on this polymer have shown excellent bioimaging properties providing excellent brightness[25,30] of the loaded fluorophore, enabling single-particle imaging inside living cells[27,31] and even detection of single molecule events at very low illumination light intensities.[32,33] Importantly, PMMA-based NPs can be loaded by various active compounds and contrast agents (including drugs).[34,35] Therefore, dye-loaded PMMA NPs appear as highly promising candidate for *in vivo* imaging down to single-particle sensitivity, but this would require rendering them "stealth" properties.

Nanoparticles placed in a biological environment have the tendency to quickly adsorb proteins non-specifically, leading to the formation of a protein corona, which then strongly determines the fate of the NP.[36–38] In consequence, a suitable surface treatment is required to provide them with so-called stealth properties in vivo.[39–42] Poly(ethylene glycol) (PEG) is the golden standard to generate stealth NPs, which prevents non-specific adsorption of proteins to surfaces and reduces elimination by reticuloendothelial system.[43–45] PEG can be implemented to the NP surface either covalently or non-covalently. The advantage of the non-covalent approach is that it does not require the use of coupling agents and additional purification steps, thus drastically simplifying formulation and decreasing risks of toxicity. Herein, we used the poloxamers pluoronic F-127 (PF-127) and F-68 (PF-68), triblockcopolymers consisting of a central, hydrophobic propylene oxide (PO) block flanked by two ethylene oxide (EO) blocks (EO:PO:EO is 95:62:95 and 81:31:81 for PF-127 and PF-68, respectively) to modify non-covalently the dye-loaded NPs. This approach has been shown to be efficient for the preparation of a PEG-shell on the surface of hydrophobic NPs.[22,26,46–49] However, it remains unclear how stable is this non-covalent hydrophobic shell in biological media. Recently, we showed that PF-68 coated polymeric NPs loaded with large drug molecule provided pharmacological effects on central nervous system (CNS) upon intravenous (iv) injection to rodents with brain trauma,[50] however the mechanism of its action is still debatable and controversial.[51]

The aim of the present study was therefore to generate polymeric nanoparticles for single-particle tracking in animals, which would combine stealth properties and exceptional brightness. At the first step, we evaluated the capacity of pluronics to protect PMMA-based NPs from non-specific interactions with proteins. In particular, using fluorescence correlation spectroscopy and Forster resonance energy transfer methods, we found that pluronics can form

a stable shell that the particle surface that cannot be easily replaced by serum proteins. Thus, the pluronic shell drastically decreased non-specific interactions with proteins. Moreover, we optimized the particle size and dye loading to obtain particles containing >15,000 donor dyes featuring 34% quantum yield, which generated ultrabright nano-objects according to two-photon fluorescence correlation spectroscopy. We found that the pluronic shell further decreased non-specific interactions with cells in culture and drastically increased the circulation time in blood. More importantly, this preparation enabled direct observation of individual NPs in brain vessels and their extravasation after brain injury. Ultrabright stealth NPs and the methodology of single particle tracking by in vivo 2-photon microscopy may therefore open new routes to better understanding the behavior of NPs in living organisms.

Materials and methods

1. Nanoparticles preparation and coating characterization

Materials

Poly(methyl methacrylate-co-methacrylic acid) (PMMA-COOH, 1,5% methacrylic acid, M_n ~15 000 and M_w ~ 34 000), poloxamer 407 (Pluronic F-127) and poloxamer 188 (Pluronic F-68), propargylamine (98%), copper(II) sulfate pentahydrate (98.0%), sodium ascorbate (>98.0%), sodium azide (99%), Triethylamine TEA, >99.5%), acetonitrile (anhydrous, 99.8%), dichloromethane (anhydrous, >99.8%), and N,N-dimethylformamide (absolute >99.8%) were purchased from Sigma-Aldrich.

N,N-diisopropylethylamine (DIPEA, >99.0%), methanesulfonyl chloride (>99.7%), and 2-aminoethane sulfonic acid (taurine, >98.0%) were obtained from TCI.

1-hydroxybenzotriazole (HOBt, >99.0%), N-tetramethyl-O-(1H-benzotriazol-1-yl)uronium hexafluorophosphate (HBTU, 99.5%), 1-[Bis(dimethylamino)methylene]-1H-1,2,3-triazolo[4,5-b]pyridinium 3-oxid hexafluorophosphate (HATU, 99.8%) were purchased from chemPrep.

Sodium phosphate monobasic (>99.0%, Sigma-Aldrich) and sodium phosphate dibasic dihydrate (>99.0%, Sigma-Aldrich) were used to prepare 20 mM phosphate buffer solutions at pH 7.4; Water was deionized using a Millipore purification system.

Synthesis

Sulfonated lissamine-alkyne. Lissamine[52],(100 mg, 0.16 mmol, 1 eq), propargylamine (11 mg, 0.19 mmol, 1.2 eq), HATU (76 mg, 0.16 mmol, 1 eq), and DIPEA (127 µL, 0.75 mmol,

5 eq) were solubilized in anhydrous DMF (5 mL) under argon. The solution was stirred under argon for 24h at room temperature. The reaction mixture was dried under reduced pressure at 65°C and then diluted with DCM (20 mL) and extracted four times with water. The combined organic phases were dried over sodium sulfate and concentrated in *vacuo*. The residue was purified by flash chromatography eluting with DCM/MeOH (99:1) to give 89.5 mg of a pink solid (yield: 54%).

^{1}H NMR (400 MHz, MeOD): δ = 8.65 (1H, s, ar. CH) + 8.03 (1H, d, ar. CH) + 7.29 (1H, d, ar. CH) + 7.16 (2H, d, ar. CH) + 6.85 (2H, d, ar. CH) + 6.73 (2H, s, ar. CH) ~9H, 3.95 (2H, s, -NCH$_2$C-), 3.51-3.65 (8H, m, -NC*H*$_2$CH$_3$), 2.45 (2H, t, -NCOCH$_2$-), 2.27 (1H, s, CCH), 1.23-1.34 (12H, m, -NCH$_2$C*H*$_3$).

Sulfonated Cy5-alkyne. To a solution of pentynyl indoleninium iodide (200 mg, 0.566 mmol) in acetic anhydride (10 mL) was added malonaldehyde dianilide hydrochloride (161 mg, 0.623 mmol, 1.1 eq). The solution was heated at 100°C for 3 h before the solvents were evaporated. To the residue was added indoleninium propanesulfonate (175 mg, 0.623 mmol, 1.1 eq) and pyridine (5 mL). The mixture was heated at 50°C for 2 h and quickly turned deep blue. The solvents were evaporated and the residue was extracted with DCM, washed with HCl (1 M) and a saturated solution of NaHCO$_3$. The organic phase was dried over anhydrous MgSO$_4$ filtered, evaporated and the crude was purified by column chromatography on silica gel (DCM/MeOH, 98/2 to 85/15) to obtain 138 mg (Yield= 45%) of the sulfonated Cy5-alkyne as a shiny deep blue solid. Rf=0.34 (DCM/MeOH: 9/1)). ^{1}H-NMR (400 MHz, DMSO-D6): δ 8.36 (m, 2H, CH), 7.61 (t, *J* = 8.4 Hz, 1H, CH Ar), 7.49 (d, *J* = 8 Hz, CH Ar), 7.42-7.34 (m, 3H, CH Ar), 7.27-7.20 (m, 2H, H Ar), 6.52 (m, 2H, 2 CH), 6.32 (d, *J* = 14 Hz, 1H, CH), 4.30 (t, *J* = 7.6 Hz, 2H, CH$_2$-N), 4.12 (t, *J* = 7.2 Hz, 2H, CH$_2$-N), 2.96 (t, *J* = 2.4 Hz, 1H, C≡CH), 2.56 (t, *J* = 6.8 Hz, 2H, CH$_2$), 2.32 (m, 2H, CH$_2$), 2.00 (m, 2H, CH$_2$), 1.87 (m, 2H, CH$_2$), 1.68 (s, 6H, 2 CH$_3$), 1.67 (s, 6H, 2 CH$_3$). ^{13}C NMR (101 MHz; CDCl$_3$): δ 173.2, 172.0, 154.5, 153.7, 142.0, 141.9, 141.1, 140.9, 128.4, 128.3, 125.7, 124.8, 124.4, 122.4, 111.3, 110.5, 103.8, 102.6, 83.4 (C≡CH), 72.1 (C≡CH), 49.0 (CH$_2$), 48.7 (CH$_2$), 47.7 (CH$_2$), 42.7 (Cq), 42.2 (Cq), 27.2 (2 CH$_3$), 27.0 (2 CH$_3$), 25.8 (CH$_2$), 23.4 (CH$_2$), 15.2 (CH$_2$). MS (ESI$^+$), calcd for C$_{33}$H$_{39}$N$_2$O$_3$ [M+H]$^+$ 543.267, found 543.240; C$_{33}$H$_{38}$N$_2$O$_3$Na [M+Na]$^+$ 565.249, found 565.186.

Dimesyl derivative of PF-127. PF-127 (6.3 g, 0.5 mmol, 1 eq) was solubilized in DCM (25 mL) and cooled to 0°C. Next, TEA (420 µL, 3 mmol, 6 eq), and methanesulfonyl chloride (234 µL, 3 mmol, 6 eq) were added. The reaction mixture was kept under stirring at 0°C for 3 h and then at room temperature overnight. The solution was dried under reduced pressure at

40°C for 30 minutes. The obtained solid was redispersed in water and purification is carried out by means of dialysis against water (48 h) to give 5.2 g of a white solid (yield: 82 %).

^{1}H NMR (400 MHz, MeOD): δ = 3.81-3.78 (4H, m, -SOCH$_2$*CH$_2$*-), 3.77-3.61 (-O*CH$_2$CH$_2$*O-) + 3.59-3.51 (m, -O*CH$_2$*CH-) + 3.43-3.38 (m, -*CH*CH$_3$) ~1000H, 3.14 (6H, s, C*H$_3$*SOO$^-$), 1.16 (~195H, m, -CH*CH$_3$*).

Diazide derivative of PF-127. The dimesyl derivative of PF-127 (5.2 g, 0.41 mmol, 1 eq) and sodium azide (165 mg, 2.46 mmol, 6 eq) were solubilized in acetonitrile (25 mL) and heated under reflux for 48 h. The obtained solid was redispersed in water and purification was carried out by means of dialysis against water (48 h) to give 4.6 g of a white solid (yield: 87%).

^{1}H NMR (400 MHz, MeOD): δ = 3.77-3.61 (-O*CH$_2$CH$_2$*O-) + 3.59-3.51 (m, -O*CH$_2$*CH-) + 3.43-3.38 (m, -*CH*CH$_3$ + *CH$_2$*N$_3$) ~1000H, 1.16 (~195H, m, -CH*CH$_3$*).

Click reaction on pluronic. The same procedure was used for the click reaction for sulfonated lissamine-alkyne and sulfonated Cy5-alkyne.

Sodium ascorbate (13 mg, 0.074 mmol, 16.5 eq in 100 µL of water) was added to a Copper(II) sulfate pentahydrate (10 mg, 0.04 mmol, 9 eq in 100 µL of water). Then the solution was added in a mixture of diazide derivative of PF-127 (55 mg, 0.0045 mmol, 1 eq), and either sulfonated lissamine-alkyne (9 mg, 0.013 mmol, 2.9 eq) or sulfonated Cy5-alkyne (7 mg, 0.013 mmol, 2.9 eq) dissolved in anhydrous DMF (5 mL). The heterogeneous mixture was stirred vigorously for 24 hours at 55°C under argon. The reaction mixture was dried under reduced pressure at 60°C, diluted in DCM, and then extracted four times with water. The combined organic phases were dried over sodium sulfate and purified by LH20 (from Sigma Aldrich) eluting with DCM/MeOH (1:1) to the final purified PF-127 conjugate with corresponding dye.

Sulfonated lissamine-alkyne PF-127 conjugate: 31 mg of a pink solid (yield: 57%), ^{1}H NMR (400 MHz, MeOD): δ = 8.65-6.70 (~11H, m, ar CH), 3.77-3.61 (-OCH$_2$CH$_2$O-) + 3.59-3.51 (m, -OCH$_2$CH-) + 3.43-3.38 (m, -CHCH$_3$) ~1000H, 1.04 (~195H, m, -CHCH$_3$); Degree of modification 61% (percentage of sulfonate lissamine-alkyne linked to pluronic).

Sulfonated Cy5-alkyne: 35 mg of blue solid (yield 80%). Degree of modification 53%.

PMMA-SO$_3$H. PMMA-COOH (300 mg, 0.045 mmol, 1 eq of COOH) was dissolved in anhydrous DCM (2 mL) under argon. Taurine (56 mg, 0.45 mmol, 10 eq), DIPEA (235 µL, 0.45 mmol, 10 eq), HOBt (61 mg, 0.45 mmol, 10 eq), and HBTU (137 mg, 0.45 mmol, 10eq) were dissolved in anhydrous DMF (3 mL) under argon, and added to the DCM solution. The solution was stirred under argon for 40 h at 40°C. The reaction mixture was dried under reduced pressure at 60°C, then the solution was precipitated in methanol. The precipitate was washed

with methanol, redissolved in acetonitrile and reprecipitated twice in methanol. After drying under vacuum 159 mg of solid were obtained (yield: 53%).

^{1}H NMR (400 MHz, $CDCl_3$): δ = 3.67 (3H, s, -CCH_3), 3.25-3.25 (0.02H, m, -NCH_2CH_2S-), 2.19-1.70 (2H, m, CCH_2); Degree of modification 77% (percentage of sulfonate groups which substituted carboxylic acid groups).

Nanoparticle preparation. Stock solutions of the polymer in acetonitrile were prepared at a concentration of 10 mg/mL. The solution was then diluted with acetonitrile to the desired concentration (1 or 4 mg/mL) and the desired amount of R18/F5-TPB was added (0, 5, or 20 wt% relative to the polymer). 50 µL of the polymer solution were then added quickly using a micropipette and under shaking (Thermomixer comfort, Eppendorf, 1100 rpm, 21°C) to 450 µL of milliQ water or milliQ water containing 4 mM NaCl. The particle solution was then quickly diluted 5-fold with water. For stabilization of NPs, different amounts of 1 or 0.1 mg/mL solutions of PF-127 or PF-68 were added under stirring to the NP solutions.

Instrumentation

NMR spectra were recorded on a Bruker Avance III 400 MHz spectrometer. The size measurements of the NPs were performed by dynamic light scattering (DLS) on a Zetasizer Nano series DTS 1060 (Malvern Instruments S.A.). It uses a laser source at 633 nm, which excludes any light excitation of our dye-doped NPs. Absorption and emission spectra were recorded on a Cary 400 Scan ultraviolet-visible spectrophotometer (Varian) and a FluoroMax-4 spectro-fluorometer (Horiba Jobin Yvon) equipped with a thermostated cell compartment, respectively. For standard recording of fluorescence spectra, the excitation wavelength was set to 530 nm and emission was recorded from 540 to 800 nm. The fluorescence spectra were corrected for detector response and lamp fluctuations.

FCS measurements were performed on a two-photon platform including an Olympus IX70 inverted microscope. Two-photon excitation at 780 nm (5 mW laser output power) was provided using a mode-locked Tsunami Ti: sapphire laser pumped using a Millenia V solid state laser (Spectra Physics). The measurements were carried out in an eight-well Lab-Tek II coverglass system, using 300 µL volume per well. The focal spot was set about 20 µm above the coverslip. The normalized autocorrelation function, G(τ), was calculated online using an ALV-5000E correlator (ALV, Germany) from the fluorescence fluctuations, δF(t), by $G(\tau) = \langle \delta F(t) \delta F(t+\tau) \rangle / \langle F(t) \rangle^2$ where t is the mean fluorescence signal and τ is the lag time. Assuming that NPs diffuse freely in a Gaussian excitation volume, the correlation function, G(τ), calculated from the fluorescence fluctuations was fitted according to Thompson[53]:

$$G(\tau)= \frac{1}{N}\left(1+\frac{\tau}{\tau_d}\right)^{-1}\left(1+\frac{1}{S^2}\frac{\tau}{\tau_d}\right)^{-1/2}$$

where τ_d is the diffusion time, N is the mean number of fluorescent species within the two-photon excitation volume, and S is the ratio between the axial and lateral radii of the excitation volume. The excitation volume is about 0.34 fL and S is about 3 to 4. The typical data recording time was 5 min, using freshly prepared PMMA NPs without further dilution. The measurements were done with respect to a reference 5(6)-carboxytetramethylrhodamine (TMR from Sigma-Aldrich) in water. The hydrodynamic diameter, d, of NPs was calculated as $d_{NPs} = \tau_{d(NPs)}/\tau_{d(TMR)} \times d_{TMR}$, where d_{TMR} is the hydrodynamic diameter of TMR (1.0 nm). The concentration of NPs was calculated from the number of species by $C_{NPs} = N_{NPs}/N_{TMR} \times C_{TMR}$, using a TMR concentration of 50 nM. NPs stability was tested by adding 10 vol% of a 10-fold concentrated PBS to the solutions of the corresponding NPs containing 10% of R18/F5 and measuring the hydrodynamic diameter and concentration. Interaction with 10% fetal bovine serum and a 1:1 mixture of 10% fetal bovine serum: PBS were tested in the same way.

2. Cell culture study

Cell culture preparation. Primary mixed cortical cell cultures were prepared from cortices of E17 Sprague Dawley rats (Charles River – kindly provided by Sabina Tahirovic) as previously described.[54] Cells were treated with DNaseI (10 µg/mL, Roche) previous to dissociation and plated at 250-300 cells/mm² in a 12-well plate containing poly-D-Lysine (0.1 mg/ml) coated glass coverslips. Cells were initially seeded in MEM supplemented with 10% FBS, 1 mM sodium pyruvate and 100 U/mL penicillin-streptomycin. After 6 hours, medium was changed to Neurobasal-A medium supplemented with 2% B-27, 2 mM GlutaMAX, 100 U/mL penicillin-streptomycin, containing in total 10 mM glucose and 1 mM pyruvate. Half of the medium was exchanged two times a week. All cell culture media/supplements from ThermoFisher, unless otherwise stated.

NPs binding to neurons in mixed cortical neuronal culture. We performed the experiments of NP attachment to neurons at DIV5, when the neuronal meshwork was not yet developed and neurons presented separate cells. We added 2 µL of bare (3 wells) or coated (3 wells) PMMA NPs into each well containing 1 mL of medium. We placed the dish under the confocal microscope in the special chamber where the temperature was set at 37˚C and CO_2 concentration at 5%. After 15 min of incubation, images of 3 different regions of interest were acquired using a Zeiss confocal microscope with 40x magnification (EC Plan-Neofluar 40x/1.30 Oil DIC M27), an image matrix of 2048 × 2048 pixel, a pixel scaling of 0.08 µm ×

0.08 µm and a depth of 16 bit. Confocal-images were collected from rhodamine and transmission light channels in plane scan mode. Fluorescent analysis was performed using FIJI software. For the dispersion analysis rhodamine channel was thresholded, binarized and processed using a particle analysis plugin. The polydispersity index (PDI) was calculated as the square of the standard deviation divided by the mean particle diameter. For the NPs binding analysis the mean grey value in rhodamine channel from the cell surface area was divided on the mean grey value in rhodamine channel from the total area. The unpaired t-test was used for statistical analysis using Graph Pad Prism 8.0.2.

NPs internalization in mixed cortical neuronal culture. We conducted the NPs internalization into neurons at DIV21/23. We added 2 µl of coated NPs into the well containing 1 mL of medium. After 1 hour of incubation, the medium was washed 3x by 0.1 M PBS and 15 min fixed with 1 mL of pre-warmed at 37˚C 4% PFA followed by 3x washing and replacing for 10 min with 1 mL of 50mM NH_4Cl then washing again and left in PBS solution at +4 ˚C until staining was performed.

Staining of the mixed cortical neuronal culture. The mixed cortical neuronal culture plated on the cover slip were permeabilized in 12-well plates with 0.1% Tween20® in 0.1 M PBS and blocked with 10 % goat serum in 0.1 M PBS. Staining was performed with 1:333 anti-GFAP (mouse, Cell Signalling Technology, #2670, Danvers, MA, USA) and anti-mouse coupled to Alexa-fluor 647 (donkey anti-mouse, Jackson Immuno Research, # 715-606-150, 1.5mg/mL in 50% glycerol) and with 1:1000 Alexa Fluor® 488 anti-Tubulin-ß3 Antibody (BioLegend®, #627905, San Diego, CA, USA). Nuclei were stained with DAPI 1:5000. Cover slips with fixed cells were directly mounted on microscope slides.

Imaging of mixed cortical neuronal culture, single cells and their analysis Confocal-images were acquired with 100x magnification (alpha Plan-Apochromat 100x/1.46 Oil DIC M27 Elyra) with an image matrix 2048x2048, a pixel scaling of 0.059 µm x × 0.059 µm and a depth of 8 bit.

3. In vivo study

Anesthesia and surgical preparation for intravital imaging. For multiphoton imaging we used an upright Zeiss LSM710 confocal microscope equipped with a Ti:Sa laser (Chameleon Vision II) from Coherent (Glasgow, Scotland) and 2 external photomultiplier detectors for red and green fluorescence. All animal experiments were conducted in accordance with institutional guidelines and approved by the Government of Upper Bavaria. 8-week old C56/Bl6N mice obtained from Charles River Laboratories (Kisslegg, Germany) were anesthetized intraperitoneally (ip) with a combination of medetomidine (0.5 mg/kg), fentanyl

(0.05 mg/kg), and midazolam (5mg/kg) (MMF). Then animals were endotracheally intubated and ventilated in a volume controlled mode (MiniVent 845, Hugo Sachs Elektronik, March-Hungstetten, Germany) with continuous recording of end-tidal pCO_2 as described previously.[55] Throughout the experiment, body temperature was monitored and maintained by a rectal probe attached to a feedback-controlled heating pad. A probe was placed in the femoral artery for measurement of mean arteriolar blood pressure and for administration of the fluorescent dye or NPs. Statistical description of physiological parameters was performed using Graph Pad Prism 8.0.2.

A rectangular 4×4-mm cranial window was drilled over the right fronto-parietal cortex under continuous cooling with saline, while special care was taken to leave the dura mater intact. The window was located 1-mm lateral to the sagittal suture and 1-mm frontal to the coronal suture. After removal of the bone flap, the dura mater was carefully removed, and the brain was rinsed with saline. Subsequently, an exact fitting rectangular cover glass of 0.175 μm thickness was placed upon the window and fixed onto the skull with dental cement. With the aim to identify the brain vessels mice were injected with FITC-dextran 3μL/g. Afterwards, mice were placed on the multiphoton microscope adapted for intravital imaging of small animals.

Kinetics of NPs in the brain vasculature. Upon scanning the baseline image, animals were administered either 7.5 μL/g of PMMA NPs (group of 3 animals) or PF-68 coated PMMA NPs (group of 5 animals), directly injected into the femoral artery. We used the 70-nm fluorescent PMMA NPs loaded with 20 wt% R18/F5-TPB at a concentration of 0.4g/L in mQ. The scanning was performed with Z-stack, 80 μm depth, laser power 3.5%-10%, 800 nm, GAASP detector with LP<570 nm filter and master gain 600 for the FITC channel and LP>570 nm for the NPs channel with master gain 530. In total, imaging time was not exceed 90 min. For the maximum depth evaluation, the scanning was performed with Z-stack, 800 μm depth, laser power 3.5%-100%, 1040 nm. The fluorescence analysis was performed using FIJI software. The Z-stack was converted to maximum intensity projection and the channels were split. The integrated density value of the each time point was divided (normalized) on the integrated density value of the baseline. To prevent fluctuation of the signal between animals, the signal from NPs channel was also divided (normalized) on FITC channel. The Two-way ANOVA statistical analysis with Tukey correction for multiple comparison was performed using Graph Pad Prism 8.0.2. The video data as well as 3D-reconstraction was prepared using Imaris® software.

Tracking the NPs outside the blood vessels. Stab injury (1 animal) was performed as described[56] during the preparation of acute cranial window for intravital imaging just before the

rectangular cover glass was placed. Lipopolysaccharide (LPS) injection (1 animal) was performed ip with the Lipopolysaccharides from Escherichia coli O55:B5 (Sigma-Aldrich, L2880-10MG) in dose 0.5mg/kg dissolved in 0.9% sterile saline as described.[57] 24 hours later the mouse was taken for the surgical preparation for the intravital imaging. Then, the mouse was placed under the 2-photon microscope and FITC-dextran was injected followed by PF-68-coated PMMA NPs. The scanning was performed with Z-stack, 250 µm depth, laser power 3.5%-22%, GAASP detector with LP<570 nm filter and master gain 600 for the FITC channel and LP>570 nm for the NPs channel with master gain 530. In total, imaging time did not exceed 60 min. For the meningeal vessels imaging, the scanning was performed every 3 seconds during 60 min, laser power 4.5 %, GAASP detector with LP<570 nm filter and master gain 600 for the FITC channel and LP>570 nm for the NPs channel with master gain 560. The video data was prepared using Zen® and Imaris® software. The particle tracking analysis was performed using FIJI with simple neurite tracer plugin. Descriptive statistics of NPs motion parameters was calculated using Graph Pad Prism 8.0.2.

Results and discussion

Formulation of nanoparticles

PMMA based NPs were assembled through nanoprecipitation (Scheme 1). In order to control their size, we used PMMA bearing a low percentage (1.1 mol%) of sulfonate groups, which was synthesized through the modification of PMMA-COOH with taurine.[26] Where needed, the salt of a rhodamine B derivative (R18) with a bulky hydrophobic counterion, tetrakis(pentafluorophenyl) borate (F5),[24] was mixed at the desired proportion with the polymer in acetonitrile before precipitation in water to obtain dye-loaded NPs. The resulting particles had a mean size of 34 nm and a low polydispersity index, as measured by DLS (Table 1). The particles loaded with 5% of R18/F5-TPB were of similar small size (36.4 nm).

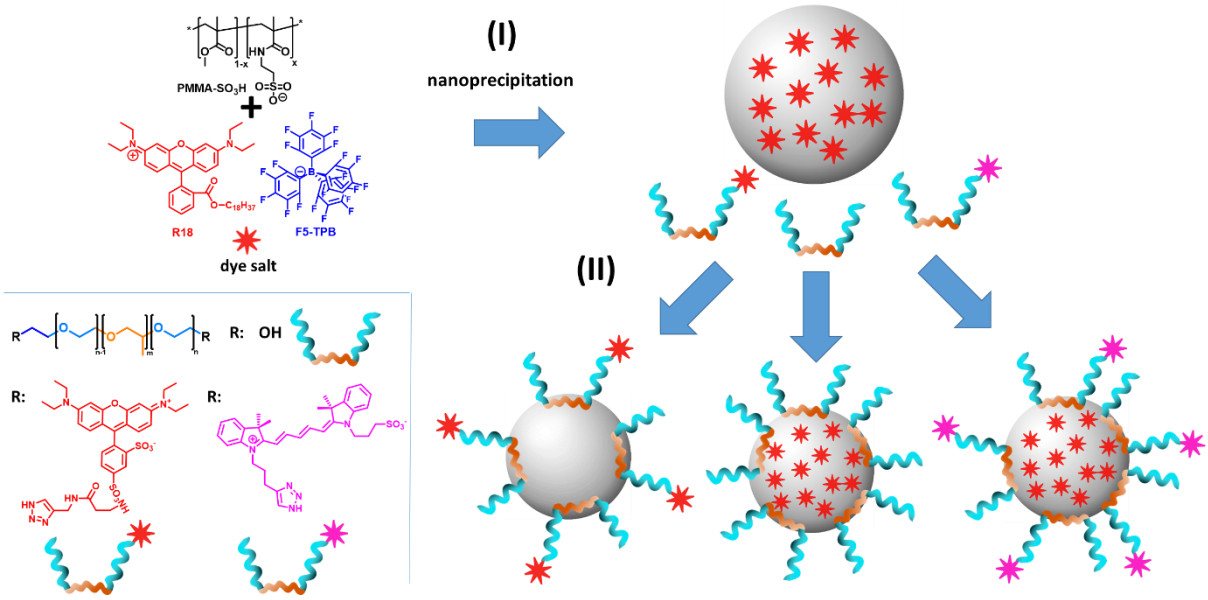

Scheme 1. Structure of the polymer PMMA-SO_3H, of the R18/F5-TPB dye salt, of the pluronics and pluronics modified with lissamine and Cy5 and preparation of the different NPs: (I) PMMA-SO_3H is mixed with the dye salt in acetontrile and precipitated in water. (II) The resulting particles are stabilized in a second step using derivatives of pluronic F-127 or pluronic F-68.

In a second step, we then added an aqueous solution of either PF-127 or PF-68 to the preformed NPs to coat them. The NP suspensions were then purified through dialysis for 48 h. DLS indicated an increase in the particle size by about 7 nm for PF-127 (and by about 4 nm for PF-68), corresponding to a surfactant corona thickness of 3.5-4 nm in good agreement with the length of the PEG-blocks. The size showed only a very small decrease upon dialysis.

Table 1. Sizes and polydispersity indices of dye-loaded NPs with and without pluronic as obtained from DLS.

Sample	Size (nm)	PDI
Bare	34.1 ± 3.1	0.118 ± 0.037
Loaded with 5wt% of R18/F5-TPB[1]	36.4 ± 2.7	0.127 ± 0.041
Coated with pluronic F-127 (before dyalisis) [1]	41.2 ± 1.8	0.141± 0.030
Coated with pluronic F-127 (after dyalisis) [1]	40.9 ± 2.5	0.133 ± 0.045
Coated with pluronic F-68 (after dyalisis) [1]	38.4 ± 3.2	0.135 ± 0.032

[1] *Prepared from 1 g/L solutions.*

Stability of Pluronics on surface of NPs studied by FRET

Förster Resonance Energy Transfer (FRET) is strongly affected by the distance between the donor and acceptor fluorophores in the range of a few nanometers.[58,59] FRET is thus a technique of choice for studying the adsorption of molecules to the surface of NPs. As donor, we selected R18 with F5-TPB as counterion, because this dye salt is highly hydrophobic and can be loaded in high amounts in PMMA NPs during nanoprecipitation.[25] Furthermore, counterion F5-TPB decrease dye self-quenching and ensures efficient donor-donor homo-FRET inside our NPs, which allows efficient FRET these donors dyes confined in the particle and an acceptor attached to the surface.[28,32,33] As acceptor, we selected specially designed neutral zwitterionic Cyanine 5 (Cy5) grafted directly at the terminal end of pluronic through 1,3-dipolar cycloaddition between pluronic bearing azide groups and Cy5 bearing alkynes. In this system FRET should thus occur only between the dye-loaded NP and pluronic adsorbed onto the particle surface **(Scheme 1)**.

We then used this system to study adsorption of pluronics on the particle surface. Different concentrations of pluronic-Cy5 were added to the uncoated R18/F5-TPB loaded NPs and we monitored the changes in the absorption and emission spectra as a function of the pluronic concentration before and after dialysis **(Figure 1, SI Figures S1, S2)**. Increase in pluronic-Cy5 concentration resulted in a gradual increase in the absorbance at 645 nm. In the fluorescence spectra, this concentration increase produced a rise in the acceptor emission at 650 nm accompanied by a decrease in the donor fluorescence at 580 nm. The latter suggests the occurrence of FRET, confirming the successful adsorption of pluronic-Cy5 on the NP surface. Interestingly, after dialysis the absorbance strongly decreased, especially for high pluronic-Cy5 concentrations, but the emission spectrum, and notably the ratio of acceptor to donor emission, only showed minor changes. This means that practically all the adsorbed pluronic remained even after 48 h of dialysis and only the free pluronic was removed during the dialysis. Thus, the pluronic shell on our polymeric NPs seems to have a quite high stability in water. On the other hand, the acceptor-donor ratio after dialysis showed a gradual increase with concentration with apparent plateau above 3000 mM of pluronic-Cy5 (Fig. 1C), which indicates that at these concentrations the particle surface is saturated with the surfactant.

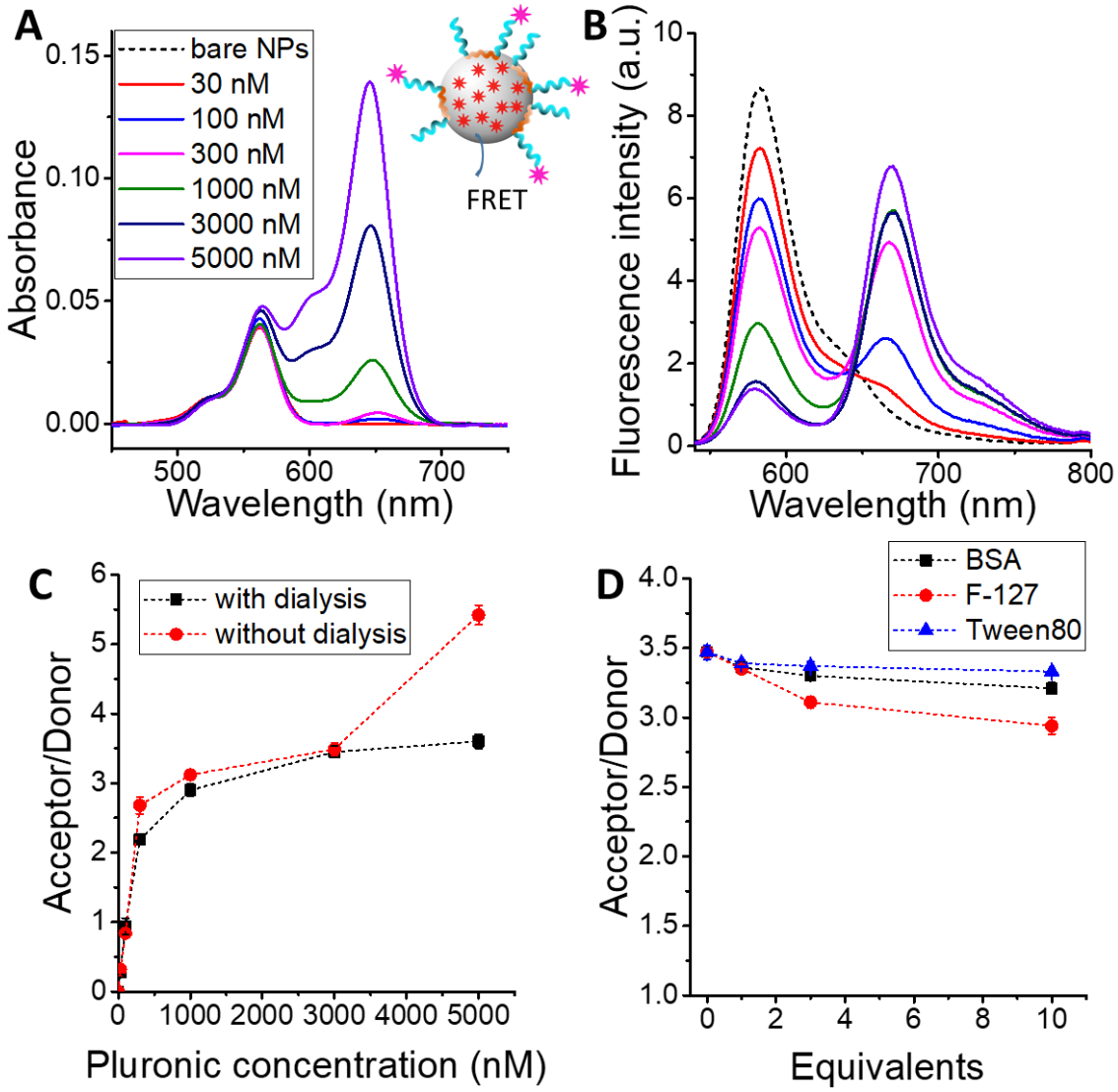

Figure 1. Adsorption of pluronic on PMMA-SO_3H NPs and their stability as studied by FRET: Absorbance (A) and emission spectra for R18/F5 loaded NPs treated with different concentrations of Cy5 bearing PF-127. (C) Ratio of the acceptor to donor emission for these NPs before and after dialysis. (D) Study of the stability against exchange of the adsorbed pluronic: The acceptor to donor ratio is given after treatment of the NPs (R18/F5 loaded NPs with 3000 nM pluronic F-127 after dialysis) for 5 min with increasing amounts of bovine serum albumine (BSA), unlabelled PF-127, or Tween80. The concentrations are given as multiples of the amount of adsorbed pluronic. Excitation 530 nm.

Since nanoparticles stabilized by pluronic shell are intended for use in multicomponent biological systems, we then evaluated the stability of the pluronic shell in presence of different competitors. We hence quantified the influence of the presence of various concentrations of three competitors, unlabeled pluronic, Tween80 and bovine serum albumin (BSA), on the FRET between the NPs and the adsorbed pluronic-Cy5 **(Figure 1D)**. The displacement of pluronic-Cy5 from the NP surface by these competitors is expected to result in a decrease of the FRET signal. All measurements have been carried out below the CMC of the surfactants in

order to minimize contributions from micelles. The NPs stabilized with pluronic did not reveal any tendency to aggregate over the whole range of competitor concentrations, as it was seen from the constant absorption spectra (data not shown). Furthermore, for all three competitors only a minor decrease in the FRET signal was observed, even at a tenfold excess of the competitors (with respect to the amount of adsorbed pluronic). This indicates a quite high stability of the adsorbed pluronic shell. Remarkably, even after 24h of incubation we detected only small decreases in FRET even for Tween80 surfactant **(Figure S3)**. Pluronic thus seems to have a particularly strong partitioning to the surface of our PMMA based NPs, leading to a quite strong fixation, which cannot be disrupted neither by surfactants nor by serum albumin.

Characterization of Pluronic Shell and NP Stability using FCS

To better characterize the adsorbed pluronic shell and its effect on NP stability, we then designed fluorescence correlation spectroscopy (FCS) experiments. FCS is a powerful method to analyze fluorescent species and notably fluorescent NPs, as it allows obtaining simultaneously information on the size, brightness and concentration of NPs or fluorescent emitters in situ.[26,60,61] FCS measures the average duration of brief burst of signal from individual fluorescence emitters diffusing through an observation volume in a confocal microscope[62].

We first used FCS to determine the number of pluronics adsorbed per NP **(Figure 2A)**. For this purpose, pluronic was modified with lissamine rhodamine dye at a concentration of 1 dye per pluronic. The labelled pluronic was then diluted with unlabeled pluronic to avoid interactions between the fluorophores. Different concentrations of this mixtures were then added to "empty" NPs without loaded dye, followed by dialysis as above. The resulting pluronic coated NPs were then analyzed by FCS. The number of pluronics per NP was then determined by measuring the brightness of the resulting NPs and comparing it to the brightness of individual lissamine labeled pluronics under the same conditions.

The quantity of pluronic molecules adsorbed on the NP surface increased with the total concentration of pluronic-lissamine (Fig. 2A). This increase was nearly linear for low concentrations of lissamine but became less pronounced above 1000 nM, indicating a Langmuir-type adsorption behavior, in line with our FRET data (Fig. 1C). At 3000 nM of pluronic, 86 pluronic molecules were adsorbed per NP. The latter corresponds to 1 PEG chain per 5.5 nm^2 of NP surface, in line with the surface per pluronic surfactant typically reported in the literature.[39 63 64]

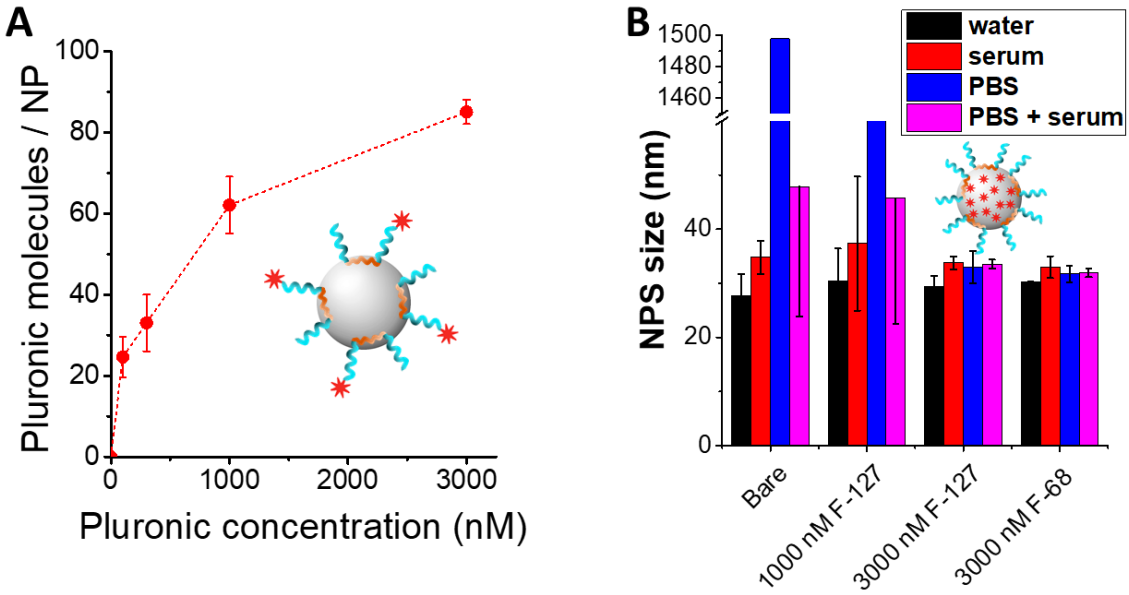

Figure 2. Adsorption and stability of pluronics on PMMA-SO_3H NPs as studied by FCS: (A) Number of pluronic molecules (labelled with lissamine) adorbed on PMMA-SO_3H NPs after dyalisis. (B) Sizes of bare NPs and NPs coated with PF-127 or PF-68 in different media.

We then studied how the pluronic shell influenced the stability of the NPs. In particular, NPs intended for biological applications should show a high colloidal stability, notably in the presence of salt, and avoid the nonspecific adsorption of proteins, leading to the formation of a protein corona [37,65]. Therefore, FCS was used to investigate the performance of our pluronic coated NPs in phosphate buffered saline (PBS), a medium mimicking ionic strength and pH of typical biological media, and in the presence of serum, which is a complex mixture of biomolecules. We monitored changes in the size distribution and concentration of bare NPs and NPs coated with two different concentrations of PF-127 and with PF-68 after incubation for 1h in the corresponding medium. NPs were loaded with R18/F5 salt (1 wt.%), which allowed us to measure by FCS their diffusion coefficient (i.e. hydrodynamic diameter), brightness, and concentration of the NPs in model biological media without any interferences due to the high concentrations of proteins in the media [66].

As shown in **Figure 2B**, the average size of NPs as measured by FCS in aqueous medium was 28 nm for bare NPs. The slightly smaller size compared to the DLS measurements stems probably from the fact that DLS is particularly sensitive to larger particles, which show higher scattering. Upon coating with pluronic the particle size increased to 32 nm, in good accordance with the thickness of the PEG-shell and DLS results. Exposing the particles to PBS resulted in fast aggregation in the case of bare particles, but also for particles coated with pluronic F-127 at a concentration of 1000 nM. By contrast, no effect of salt on the size was observed for NPs

coated at a concentration of 3000 nM with either PF-127 or PF-68. Thus, only at 3000 mM of pluronics, it shields the entire particle surface (according FRET and FCS data), the surfactant renders NPs stable against aggregation in saline solution. When exposed to a 10% serum solution, the size of bare NPs increased by about 10 nm, corresponding to the adsorption of at least a monolayer of serum proteins. In the case of NPs treated with 1000 or 3000 nM of PF-127, this effect was negligible (<2 nm of size increase). The size increase upon exposure to serum proteins was even less pronounced (<1 nm) for particles coated with 3000 nM PF-68.

Pluronic, being amphiphilic block copolymers, thus adsorbed strongly onto the surface of our hydrophobic NPs via their hydrophobic polyoxypropylene (POP) center block. In this way the hydrophilic polyoxyethylene (PEG) blocks form a brush layer on the particle surface. Once a sufficient density of this PEG brush is reached, it provided particle stability vs particle aggregation in saline solutions and prevented adsorption of serum proteins, presumably through steric repulsion.[67] The slightly higher protein resistance of NPs coated with PF-68 is probably due to the higher PEG content of the later, leading to a denser brush. For this reason, PF-68 was chosen for *in vivo* experiments.

Optimization of particle brightness

In order to detect NPs at the single-particle level in vivo, the rational way is to increase the number of dyes per particle by increasing the particle size and the dye loading. As the nanoprecipitation of our polymers is controlled by their charge,[26] the particle size should depend on the ionic strength (i.e. salt concentration).[27] We found that the gradual increase in salt concentration resulted in an increase in the particle size from 44 nm up to 126 nm, according to DLS, while maintaining good polydispersity (Table 2). Moreover, the dye loading was increased to 20 wt%, which according to our earlier studies,[25,32] could be optimal to preserve high fluorescence quantum yield of encapsulated dyes without significant self-quenching. Indeed, the fluorescence quantum yield was relatively high (32-36%) for all studied particle sizes.

Then, we evaluated the single-particle properties using fluorescence correlation spectroscopy. As our particles were designed for two-photon intravital imaging, the two-photon excitation source was used to evaluate the single-particle brightness. As a standard we chose polymeric beads loaded with Nile Red (FluoSpheres, FS), exhibiting absorption and emission at similar wavelengths. According to provider information and our measurements, these beads showed extinction coefficient 5.4×10^8 M^{-1} cm^{-1}, which corresponded to ~120 encapsulated Nile Red dyes per NP. According to our two-photon FCS, the single-particle brightness of our smallest

tested NPs (44 nm) was equivalent to 41 FS particles while exhibiting similar hydrodynamic diameter (39 nm, Table 2). This striking difference is related to much stronger loading of our NPs, which theoretically should contain ~2000 rhodamine B dyes (vs 120 Nile Red in case of FS) as well as difference of rhodamine B (200 GM)[68] *vs* Nile Red (32 GM) [69] in the two-photon absorption cross-section at 830 nm.

Besides, the size increase of our NPs led to a further increase in brightness (Table 2). For most NPs, the size measured by DLS matched well that obtained by FCS, except for the largest NPs, probably due to their larger polydispersity. Therefore, our best formulation combining large size, good polydispersity and high brightness was the 74-nm NPs, which were 150 times brighter than FS particles.

Table 2. Effect of salt on the size and fluorescence quantum yield of NPs.

Concentration of NaCl, mM	Size, nm DLS	Poly-dispersity	QY, %	Size, nm FCS	BR, FCS
FluoSpheres®	39	0.25	28	39	1
5	44	0.078	32	48	40.5
7	47	0.096	35	47	42.7
10	51	0.082	36	49	57.6
15	59	0.094	36	60	82.7
25	74	0.116	34	73	150
50	126	0.134	34	75	246

In vivo Imaging of Pluronic Coated NPs.

As the next step, we took advantage of the high brightness of these dye-loaded polymeric NPs to get a better understanding of their interaction with biological systems, particularly in the brain. Despite many studies evaluating polymeric NPs as drug-carriers to the brain, their tracking with a single-particle resolution, so far, remained an unsolved challenge. The main question we addressed was to track a single nanoparticle from the vessels to the brain parenchyma and analyse their interactions with the related tissues and cells, like blood, endothelial cells, blood-brain barrier, macrophages, and neurons. To achieve this, we selected the brightest particles obtained herein, which is the 74 nm NPs loaded with 20 wt% of R18/F5-TPB.

Neuronal binding and uptake of NPs.

First, we wanted to test the possibility of tracking NPs in cell culture and understand their interaction with primary dissociated cortical neurons. **(Figure 3A)**. We first performed experiments on young (5 days in vitro (DIV)) neurons **(Figure 3B)**. After adding NPs into the cell culture, we could easily detect the particles, which hovered in the media. This allowed us to track individual particles and quantify their motion, aggregation, and location with only real-time confocal imaging. Notably, bare NPs seeded in 15 minutes, while PF-68-coated NPs remained floating in the media during all the observation time (up to 30 minutes). Moreover, bare NPs displayed heterogeneous aggregates with inconsistent shapes and brightness **(Figure 3B)**, while PF-68-coated NPs appeared as homogenous and uniform foci. Furthermore, the polydispersity index (PDI) of coated NPs was between 0.1-0.2 confirming their higher stability in the media while the PDI of bare NPs was above 0.6-0.8 indicating aggregation ($p=0.0137$) **(Figure 3C)**. These data in line with FRET and FCS data indicated that coating of NPs by PF-68 provided stability in the cell culture media

Next, we checked the interaction of the particles with the cell surface. During the first 15 minutes, we observed NPs on the neuronal surface in both groups; however, bare NPs where much more numerous, as depicted by the very high fluorescent intensity ($p<0.0001$) **(Figure 3D)**. This effect is likely due the strong nonspecific binding of bare polymeric NPs and the negative charges which contribute to binding to neurons, as recently shown for QDs on primary hippocampal culture.[71]

Then, we evaluated whether the NPs could be up-taken by neurons. We exploited matured (21 DIV) mixed cortical neurons that already have a formed dense network confluent astrocyte layer **(Figure 3E)**. The Cells were transduced with Adeno-associated virus expressing the calcium sensor Gcamp7. We first verified that the cultures were healthy and able of firing by measuring neuronal activity in presence of NPs in the media **(Suppl_movie_S01)**. Next, we analysed the behaviour of the NPS. We found that after 60 minutes PF-68-coated NPs were internalized by neurons. We could resolve the localization at subcellular resolution and identify the presence of individual NPs distributed along the processes and accumulated in the cell soma. We did not observe uptake from astrocytes **(Figure 3E)**. The neuronal phagocytosis is a well-known process mostly related with the clearance of debris in the brain parenchyma. Indeed, internalization of various compounds like myelin, cell debris, protein aggregates and microspheres was reported in different types of neurons.[72]

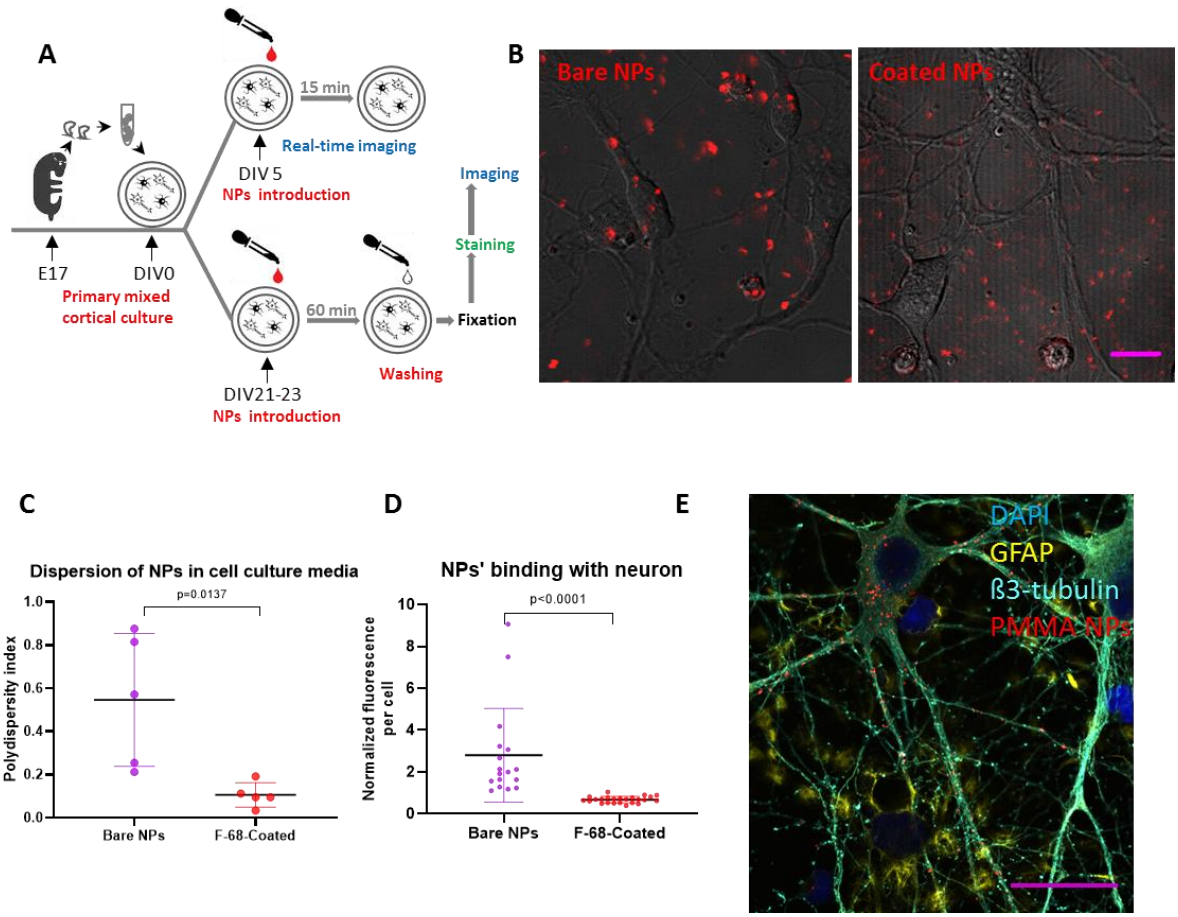

Figure.3. **Neuronal uptake and binding of bare and coated NPs**. **A:** experimental pipeline from preparation of mixed cortical neuron cell culture dissociated from an E17 rat embryo to acquisition of NPs and their cellular uptake. DIV, days *in vitro*. **B:** A representative confocal plane scan of the ROI of neuronal cell culture 15 minutes after the treatment by bare or coated NPs. **C,D:** Quantification of the **Fig.1B** was analyzed using FIJI software. For the dispersion, the "analysis particles" plugin was utilized, while for the NPs-cell binding, the rhodamine signal from each neuron was normalized to the total signal. For the statistical analysis, unpaired t-test was used (each group contained 3-5 dishes, each dish 3-4 ROI). Data presented as means ± standard deviation (SD). **E**: a confocal plane scan of neuronal uptake of coated NPs, 60 minutes after the treatment. Neurons labeled by ß3-tubulin and astrocytes – by GFAP. The neuron is internalized with coated NPs surrounded by NPs-free astrocytes. Scale bar: magenta – 10 µm.

Detection of single particles and their circulation kinetics in the blood vessels.

The next step was to demonstrate the potential use of the NPs in the live animal.

We therefore investigated the stability and circulation kinetics of the NPs injected in the blood stream. We performed live imaging by 2-photon microscopy (2PM) of a mouse brain implanted with an acute cranial window. The NPs as well as FITC-dextran (2000 kD) labelling the cerebral vessels were delivered through a femoral catheter during imaging **(Figure 4A)**. Importantly, NPs injection and imaging conditions did not affect the physiological parameters

of the animals **(Suppl_Table_S1)**. We identified the brain vessels and selected the region containing all types, namely the pial, penetrating vessels, arterioles, venules and capillaries **(Figure 4C, Baseline)**. We found that during live imaging both bare and PF-68-coated NPs solutions were clearly detectable in the mouse brain vasculature **(Figure 4B)**. Important to note that fluorescent signal from the FITC-dextran was homogenous, while NPs appeared as discrete spots. While circulating bare NPs formed heterogeneous aggregates with different brightness, the PF-68-coated NPs appeared mono-disperse. The fluorescent level and separation of individual particles enabled to track their trajectories in the blood vessels **(Suppl_Movie_S02)** and acquired images with high signal to noise ratio up to 800 μm depth **(SI Figure S4)**. Next, we did one-hour- timelapse imaging of NPs in blood circulation. We found that as early as 15 minutes post-injection the signal from bare NPs drastically decreased and could only be detected in large vessels **(Figure 4C),** indicating that bare NPs were immediately eliminated out of the blood stream. In sharp contrast, PF-68-coated NPs were easily detectable during all the imaging time (60 min) both in capillaries and in larger vessels **(Figure 4C)**. Additionally, NPs were secluded in blood vessels and were not detected in the cortical brain parenchyma.

Image analysis showed significant increase in a relative fluorescence intensity of coated NPs compared to the bare at all studied time points **(Figure 4D)**. The rate of fluorescence decay corresponded to the elimination rate of NPs from the blood indicating that PF-68-coated NPs half-life was around 40 minutes (**Figure 4D**). Thus, we successfully demonstrated real-time two-photon imaging at high resolution of single circulating polymeric NPs in brain blood vessel that was not achieved so far. (ref to add [*https://www.nature.com/articles/srep04279; https://onlinelibrary.wiley.com/doi/10.1002/adma.201301938*)

Though the stealth effect of NPs coated by pluoronics has been already presented previously,[49] our findings shows the effect of pluronics coating at the single-particle level, which provide direct information about the particle behaviour in vivo. On the other hand, pluronics was also reported to assist delivery of large molecules into the brain,[51] however we could not detect any particles outside the brain vasculature throughout the whole observational period implicating that carrier was not transferred through the BBB.

As PMMA NPs could also serve as a model nanocarrier of drugs, our data is a robust base for future discovery of drug carriers in microvascular flow real-time *in vivo*, i.e. blood circulation kinetics, marginalization inside the vessels, penetration through the blood-brain barrier and brain biodistribution.

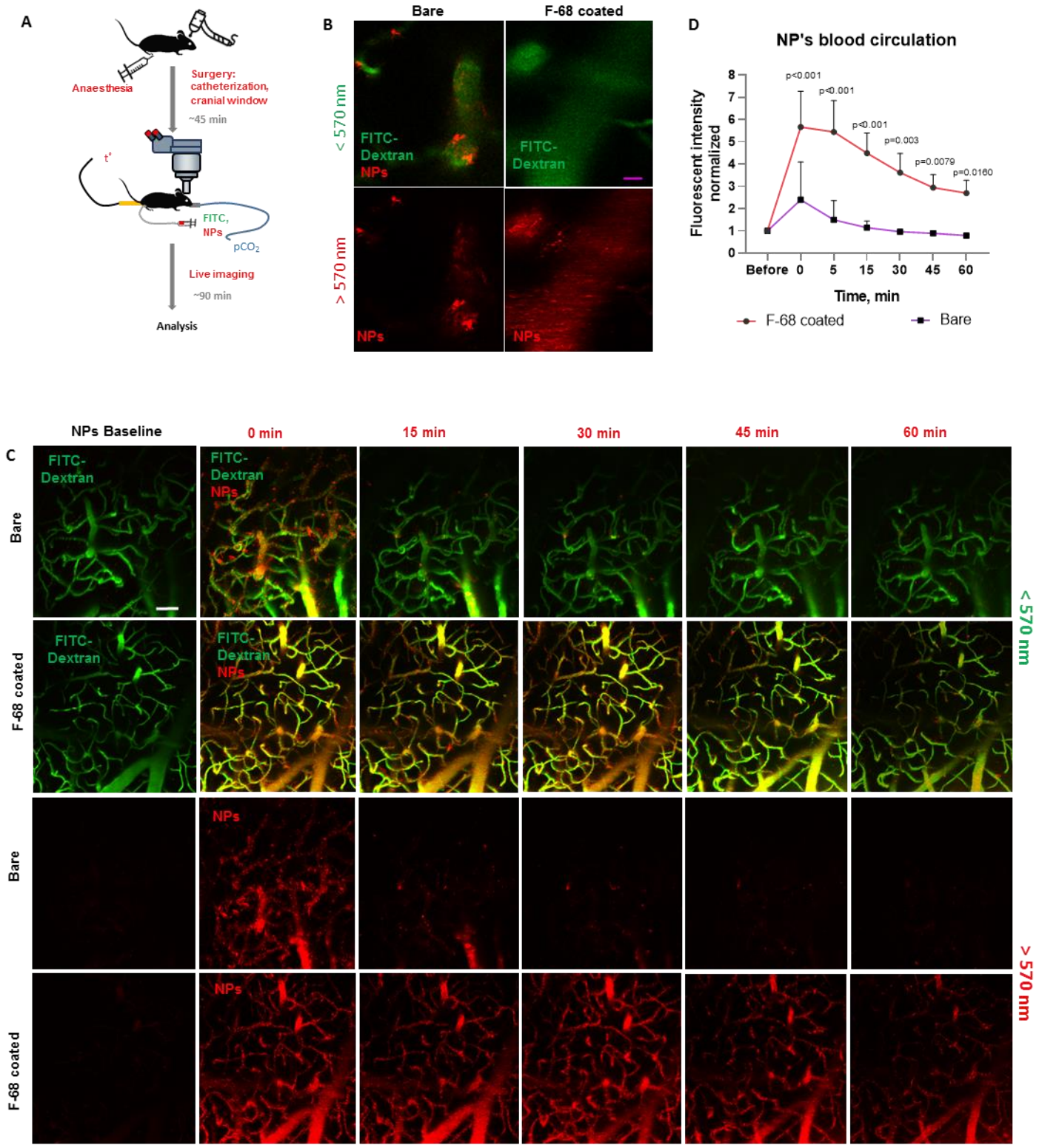

igure 4. **Intravital 2-photon microscopy of NPs in the mouse brain vasculature**. **A**: Experiment design of preparation of animal to intravital imaging, duration of imaging. **B**: Single particles trajectories. Scanned images 5 min after injection of NPs solution. Z-stack, 80 µm depth, maximum intensity projection. Laser power 3.5%-10%. Scale bar - 10 µm. **C:** Scanned images immediately after injection of FITC-dextran (NP baseline) or NPs solution during 0-60min. The two upper raws are the merged green (FITC-dextran) and red (NPs) channels; the

two lower – only red (NPs) channel. Z-stack, 80 µm depth, maximum intensity projection. Scale bar - 50 µm. **D**: Quantification of the circulating kinetics, analyzed using FIJI. Data presented as means ± SD. For the statistical analysis, Two-way ANOVA between coated and bare NPs was used with Tukey correction for multiple comparison (bare NPs n=3, coated NPs n=5).

Real-time extravasation and cellular uptake of single NPs in alive animals.

To analyse further the fate of NPs circulating in the blood we first tracked them in extra-cerebral vessels, like meningeal vessels which are devoided of BBB (https://doi.org/10.1016/j.ymeth.2017.03.020).

Using the same experimental setup **(Figure 4A),** we focused our imaging on meningeal vessels that were clearly seen after injection of FITC-dextran **(Figure 5B)**. Upon injection we could immediately detect the NPs inside meningeal vessels **(Figure 5B).** 30 minutes later, we observed diffuse extravasation of coated-NPs. Importantly extravased NPs in the meningeal interstitium and epidural space displayed typical Brownian movement highlighting the single-particle resolution **(Suppl_Movie_S03)** . Quantitative analysis of the tracking showed the motion of individual NPs from the vessel to the macrophage **(Figure 5C, Table 3)**. The particles reaching the meningeal macrophages were uptaken and for the vast majority became internalized 60 minutes after injection. These events were not observed with the bare NPs probably due to their fast elimination **(Suppl_Movie_S04).**

The implantation of cranial window at the time of imaging triggers transient inflammation due the surgical intervention. To control for this parameter, we let the animals recover for 4 weeks prior imaging (chronic cranial window). In this condition, we did not observe extravasation of NPs **(Suppl_Movie_S05**). Therefore inflammatory state facilitates the extravasation of NPs also reported as enhanced permeability and retention (EPR) .[74]

Neuroinflammation is a hallmark of neurological diseases and associated with BBB leakage (https://doi.org/10.3389/fphar.2019.01008). This phenomenon could therefore be used advantageously for NPs targeting of brain parenchyma. To this end, we used two different approaches:, local injury and systemic inflammation **(Figure 5A)**.

First, we used cortical stab wound injury, a small-sized model of brain damage without massive bleeding enabling imaging through the cranial window. After the stab injury we found extravasated NPs accumulating along the axis of injury in all types of the vessels but confined to the site of the injury **(Figure 5E, Suppl_Movie_07)**,

We and others already applied the NPs after traumatic brain injury [81 82 50], however the extravasation was never shown as in this study in alive animal.

Second, we induced systemic inflammation by intraperitoneal injection of lippopolysaccharide (LPS) 24 hours before the imaging **(Figure 5A)**. LPS, a gram-negative endotoxin, causes severe systemic inflammatory response with cytokine activation through LPS-binding proteins and CD14.[75] LPS derived from *E. coli* 055:B5 was used , as it was reported to open the BBB in many studies.[76,77]

During intravital imaging, LPS-injected mice presented an extravasation of NPs from the brain parenchymal vessels, predominantly, in capillary level, indicating an opening of cortical BBB sufficient for our NPs of 74-nm size. At 20 minutes post-injection, extravasation of NPs could already detected **(Figure 5D, Suppl._Movie_S06)**. Moreover, the amount of the foci of extravasation was gradually increasing until the end of the imaging session indicating accumulation of NPs. Despite many studies on LPS-induced BBB opening,[78–80], the present data is the first demonstration of LPS-induced crossing of the BBB by NPs in real-time *in vivo*.

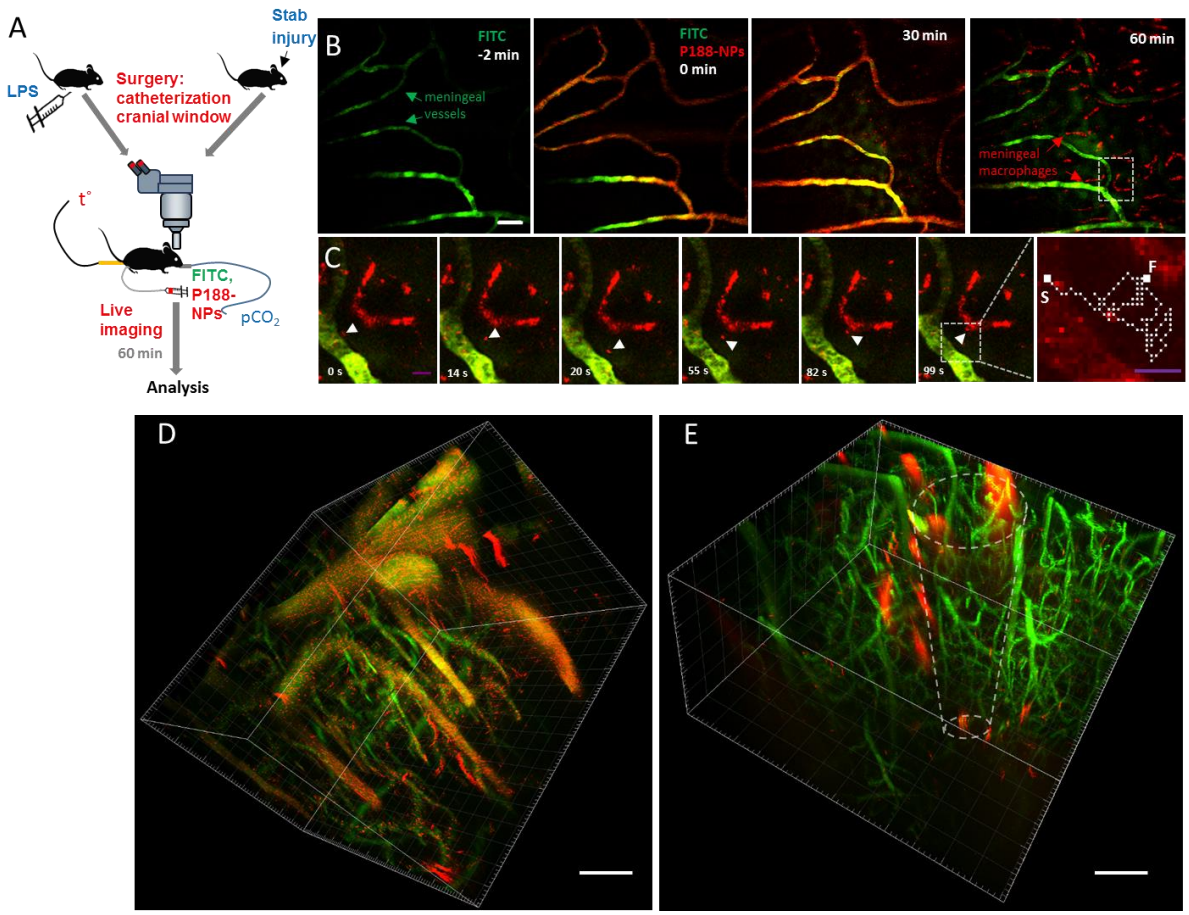

Figure 5. **The tracking of NPs outside the vessels in alive animal**. **A**: Experiment design from a mouse injected with LPS 24 hours before the intravital imaging and a mouse with a stab injury made during preparation of acute cranial window. Duration and conditions of imaging. **B**: A single plane of merged channels from the time series scans of meningeal vessels (**Suppl. Movie S05.**) of a mouse (experimental design as in **Figure 3A**) with acute cranial window before and 60 minutes after injection of coated NPs. Green indicates meningeal vessels (FITC-

dextran), red foci – NPs; red line-shaped spots – an uptake of NPs by meningeal macrophages. **C:** Tracking of the NP from the vessel to the macrophage during 99s. White arrow – single particle. Selected by white lines – a zoomed area in between vessel (S- start) and meningeal macrophage (F – finish). White dotty line is a trajectory of NP quantified as follows, path: 165.3±75.0 µm; mean branch: 3.0±0.1 µm; longest branch: 14.1±1.3 µm; speed: 2.1±0.5 µm/s. Erros is standard deviation (n=6). **D, E**: A 3D reconstruction of *In vivo* 2PM rendered z-stack 0-250 µm of the coated NPs and FITC-dextran circulating in the brain vasculature of mouse injected with LPS or injured focally. 20 minutes after injection of NPs. Green indicates brain vessels, red foci that are non-co-locolazed with the green, indicates the sites of NPs extravasation. Z-stack, 250 µm depth. Scale bar: white - 50 µm; Magenta – 5 µm.

Table.3 NP's extravasation-uptake motion parameters m±SD (n=6).

165.3±75.0	3.0±0.1	14.1±1.3	2.1±0.5
Path, µm	Mean branch, µm	Longest branch, µm	Speed, µm/s

Conclusion

Monitoring organic nanoparticles *in vivo* at the single particle level remains a big challenge, which could greatly improve our understanding of bottlenecks in the field of nanomedicine, offering new directions in theranostics. For this purpose, particles should have two key features: stealth properties to remain sufficiently long in the blood circulation and extreme brightness to be detected despite fast circulation velocities/short exposure times and strong background. Here, we addressed these issues using dye-loaded polymeric nanoparticles (NPs), composed of the hydrophobic polymer PMMA-SO_3H loaded with a dye resistant to self-quenching: octadecyl rhodamine B with bulky hydrophobic counterion that insulates fluorophores from aggregation. In a first step, using UV-visible, FRET and FCS methods, we demonstrated that PEGylated amphiphilic block copolymers, such as pluronic F-68 and F-127, can adsorb at the surface of PMMA-SO_3H polymeric NPs, so that after dialysis 1 amphiphile per 5.5 nm^2 remains bound to NP surface. The pluronic shell is also found resistant to displacement by serum proteins or surfactants. As a result, the simple adsorption of pluronics rendered these initially hydrophobic NPs stable in physiological environments providing them stealth properties against non-specific protein adsorption. Pluronics coating also minimize non-specific interactions with neurons in cell culture. Second, to achieve extreme brightness, we increased particle size by increasing salt concentration in the medium for nanoprecipitation of the charged polymer. According to two-photon FCS, our optimized NPs of 74-nm

hydrodynamic diameter loaded at 20 wt% of the rhodamine dye salt were 150-fold brighter than commercial Nile Red-loaded FluoSpheres™ of 39 nm diameter. This high fluorescence brightness combined with stealth properties of the obtained dye-loaded polymeric NPs made it possible to track single particles directly in the cerebral vasculature of the mouse, which has been a challenge so far. Thereby, our data is a robust base for future monitoring of the behaviour of drug carriers in the microvasculature of living animals. Furthermore, by employing ultrabright polymeric NPs it is possible to precisely analyse their blood circulation kinetics and biodistribution, including crossing the blood-brain barrier in real-time. In particular, we showed that a single PMMA NP can be tracked and quantified from the time of its injection until its uptake by meningeal macrophages, a process which has so far not been demonstrated in living animals. Using these NPs we further directly demonstrated opening of the BBB after systemic inflammation and physical brain injury *in vivo*.

The use of the currently developed ultrabright NPs pushes the boundary of the detection of NPs' in living organisms significantly thus allowing rapid and precise assessment of the biodistribution and bioavailability of NPs *in vivo*. The current study demonstrates how the combination of nanoparticle design and the latest imaging technologies can help to enhance the precision of nano-formulation and nano-biodistribution thereby providing direct evidence how NPs cross biological barriers and distribute within living tissue.

Acknowledgement

This project has received funding from the Alexander von Humboldt Foundation, European Union's Horizon 2020 research and innovation programme under the Marie Skłodowska-Curie grant agreement No 794094, Synergy Munich Cluster and ERA-NET Neuron. We thank Mihail Todorov for assisting in imaging analysis.

References:

(1) Schwartz, R. S. Paul Ehrlich's Magic Bullets. *N. Engl. J. Med.* **2004**, *350* (11), 1079–1080. https://doi.org/10.1056/NEJMp048021.

(2) Flühmann, B.; Ntai, I.; Borchard, G.; Simoens, S.; Mühlebach, S. Nanomedicines: The Magic Bullets Reaching Their Target? *Eur. J. Pharm. Sci.* **2019**, *128*, 73–80. https://doi.org/10.1016/j.ejps.2018.11.019.

(3) Rodallec, A.; Benzekry, S.; Lacarelle, B.; Ciccolini, J.; Fanciullino, R. Pharmacokinetics Variability: Why Nanoparticles Are Not Just Magic-Bullets in Oncology. *Crit. Rev. Oncol. Hematol.* **2018**, *129*, 1–12. https://doi.org/10.1016/j.critrevonc.2018.06.008.

(4) Hendricks, W. P.; Yang, J.; Sur, S.; Zhou, S. Formulating the Magic Bullet: Barriers to Clinical Translation of Nanoparticle Cancer Gene Therapy. *Nanomed.* **2014**, *9* (8), 1121–1124. https://doi.org/10.2217/nnm.14.63.
(5) Wilhelm, S.; Tavares, A. J.; Dai, Q.; Ohta, S.; Audet, J.; Dvorak, H. F.; Chan, W. C. W. Analysis of Nanoparticle Delivery to Tumours. *Nat. Rev. Mater.* **2016**, *1* (5), 1–12. https://doi.org/10.1038/natrevmats.2016.14.
(6) Zhou, Z.; Yang, L.; Gao, J.; Chen, X. Structure–Relaxivity Relationships of Magnetic Nanoparticles for Magnetic Resonance Imaging. *Adv. Mater.* **2019**, *31* (8), 1804567. https://doi.org/10.1002/adma.201804567.
(7) Gao, X.; Guo, L.; Li, J.; Thu, H. E.; Hussain, Z. Nanomedicines Guided Nanoimaging Probes and Nanotherapeutics for Early Detection of Lung Cancer and Abolishing Pulmonary Metastasis: Critical Appraisal of Newer Developments and Challenges to Clinical Transition. *J. Controlled Release* **2018**, *292*, 29–57. https://doi.org/10.1016/j.jconrel.2018.10.024.
(8) Lusic, H.; Grinstaff, M. W. X-Ray-Computed Tomography Contrast Agents. *Chem. Rev.* **2013**, *113* (3), 1641–1666. https://doi.org/10.1021/cr200358s.
(9) Guo, C.; Jin, Y.; Dai, Z. Multifunctional Ultrasound Contrast Agents for Imaging Guided Photothermal Therapy. *Bioconjug. Chem.* **2014**, *25* (5), 840–854. https://doi.org/10.1021/bc500092h.
(10) Chen, M.; Yin, M. Design and Development of Fluorescent Nanostructures for Bioimaging. *Prog. Polym. Sci.* **2014**, *39* (2), 365–395. https://doi.org/10.1016/j.progpolymsci.2013.11.001.
(11) Schuster, B. S.; Ensign, L. M.; Allan, D. B.; Suk, J. S.; Hanes, J. Particle Tracking in Drug and Gene Delivery Research: State-of-the-Art Applications and Methods. *Adv. Drug Deliv. Rev.* **2015**, *91*, 70–91. https://doi.org/10.1016/j.addr.2015.03.017.
(12) Peng, H.-S.; Chiu, D. T. Soft Fluorescent Nanomaterials for Biological and Biomedical Imaging. *Chem. Soc. Rev.* **2015**, *44* (14), 4699–4722. https://doi.org/10.1039/C4CS00294F.
(13) Zhou, Y.; Peng, Z.; Seven, E. S.; Leblanc, R. M. Crossing the Blood-Brain Barrier with Nanoparticles. *J. Controlled Release* **2018**, *270*, 290–303. https://doi.org/10.1016/j.jconrel.2017.12.015.
(14) Kilin, V. N.; Anton, H.; Anton, N.; Steed, E.; Vermot, J.; Vandamme, T. F.; Mely, Y.; Klymchenko, A. S. Counterion-Enhanced Cyanine Dye Loading into Lipid Nano-Droplets for Single-Particle Tracking in Zebrafish. *Biomaterials* **2014**, *35* (18), 4950–4957. https://doi.org/10.1016/j.biomaterials.2014.02.053.
(15) Estelrich, J.; Sánchez-Martín, M. J.; Busquets, M. A. Nanoparticles in Magnetic Resonance Imaging: From Simple to Dual Contrast Agents. *Int. J. Nanomedicine* **2015**, *10*, 1727–1741. https://doi.org/10.2147/IJN.S76501.
(16) Jin, D.; Xi, P.; Wang, B.; Zhang, L.; Enderlein, J.; van Oijen, A. M. Nanoparticles for Super-Resolution Microscopy and Single-Molecule Tracking. *Nat. Methods* **2018**, *15* (6), 415–423. https://doi.org/10.1038/s41592-018-0012-4.
(17) Handbook of Fluorescence Spectroscopy and Imaging: From Ensemble to Single Molecules | Wiley https://www.wiley.com/en-us/Handbook+of+Fluorescence+Spectroscopy+and+Imaging%3A+From+Ensemble+to+Single+Molecules-p-9783527316694 (accessed Feb 4, 2020).
(18) Sauer, M.; Heilemann, M. Single-Molecule Localization Microscopy in Eukaryotes. *Chem. Rev.* **2017**, *117* (11), 7478–7509. https://doi.org/10.1021/acs.chemrev.6b00667.
(19) Wolfbeis, O. S. An Overview of Nanoparticles Commonly Used in Fluorescent Bioimaging. *Chem. Soc. Rev.* **2015**, *44*, 4743–4768. https://doi.org/10.1039/C4CS00392F.

(20) Wu, C.; Chiu, D. T. Highly Fluorescent Semiconducting Polymer Dots for Biology and Medicine. *Angew. Chem. Int. Ed Engl.* **2013**, *52* (11), 3086–3109. https://doi.org/10.1002/anie.201205133.
(21) Reisch, A.; Klymchenko, A. S. Fluorescent Polymer Nanoparticles Based on Dyes: Seeking Brighter Tools for Bioimaging. *Small* **2016**, *12* (15), 1968–1992. https://doi.org/10.1002/smll.201503396.
(22) Li, K.; Liu, B. Polymer-Encapsulated Organic Nanoparticles for Fluorescence and Photoacoustic Imaging. *Chem Soc Rev* **2014**, *43* (18), 6570–6597. https://doi.org/10.1039/C4CS00014E.
(23) Mei, J.; Leung, N. L. C.; Kwok, R. T. K.; Lam, J. W. Y.; Tang, B. Z. Aggregation-Induced Emission: Together We Shine, United We Soar! *Chem. Rev.* **2015**, *115* (21), 11718–11940. https://doi.org/10.1021/acs.chemrev.5b00263.
(24) Reisch, A.; Didier, P.; Richert, L.; Oncul, S.; Arntz, Y.; Mély, Y.; Klymchenko, A. S. Collective Fluorescence Switching of Counterion-Assembled Dyes in Polymer Nanoparticles. *Nat. Commun.* **2014**, *5*, 4089. https://doi.org/10.1038/ncomms5089.
(25) Reisch, A.; Trofymchuk, K.; Runser, A.; Fleith, G.; Rawiso, M.; Klymchenko, A. S. Tailoring Fluorescence Brightness and Switching of Nanoparticles through Dye Organization in the Polymer Matrix. *ACS Appl. Mater. Interfaces* **2017**, *9* (49), 43030–43042. https://doi.org/10.1021/acsami.7b12292.
(26) Reisch, A.; Runser, A.; Arntz, Y.; Mély, Y.; Klymchenko, A. S. Charge-Controlled Nanoprecipitation as a Modular Approach to Ultrasmall Polymer Nanocarriers: Making Bright and Stable Nanoparticles. *ACS Nano* **2015**, *9* (5), 5104–5116. https://doi.org/10.1021/acsnano.5b00214.
(27) Reisch, A.; Heimburger, D.; Ernst, P.; Runser, A.; Didier, P.; Dujardin, D.; Klymchenko, A. S. Protein-Sized Dye-Loaded Polymer Nanoparticles for Free Particle Diffusion in Cytosol. *Adv. Funct. Mater.* **2018**, *28* (48), 1805157. https://doi.org/10.1002/adfm.201805157.
(28) Melnychuk, N.; Klymchenko, A. S. DNA-Functionalized Dye-Loaded Polymeric Nanoparticles: Ultrabright FRET Platform for Amplified Detection of Nucleic Acids. *J. Am. Chem. Soc.* **2018**, *140* (34), 10856–10865. https://doi.org/10.1021/jacs.8b05840.
(29) Oonishi, H.; Akiyama, H.; Takemoto, M.; Kawai, T.; Yamamoto, K.; Yamamuro, T.; Oonishi, H.; Nakamura, T. The Long-Term in Vivo Behavior of Polymethyl Methacrylate Bone Cement in Total Hip Arthroplasty. *Acta Orthop.* **2011**, *82* (5), 553–558. https://doi.org/10.3109/17453674.2011.625538.
(30) Rosiuk, V.; Runser, A.; Klymchenko, A.; Reisch, A. Controlling Size and Fluorescence of Dye-Loaded Polymer Nanoparticles through Polymer Design. *Langmuir* **2019**, *35* (21), 7009–7017. https://doi.org/10.1021/acs.langmuir.9b00721.
(31) Runser, A.; Dujardin, D.; Ernst, P.; Klymchenko, A. S.; Reisch, A. Zwitterionic Stealth Dye-Loaded Polymer Nanoparticles for Intracellular Imaging. *ACS Appl. Mater. Interfaces* **2020**, *12* (1), 117–125. https://doi.org/10.1021/acsami.9b15396.
(32) Trofymchuk, K.; Reisch, A.; Didier, P.; Fras, F.; Gilliot, P.; Mely, Y.; Klymchenko, A. S. Giant Light-Harvesting Nanoantenna for Single-Molecule Detection in Ambient Light. *Nat. Photonics* **2017**, *11* (10), 657–663. https://doi.org/10.1038/s41566-017-0001-7.
(33) Melnychuk, N.; Egloff, S.; Runser, A.; Reisch, A.; Klymchenko, A. S. Light-Harvesting Nanoparticle Probes for FRET-Based Detection of Oligonucleotides with Single-Molecule Sensitivity. *Angew. Chem. n/a* (n/a). https://doi.org/10.1002/ange.201913804.
(34) Cardoso Dos Santos, M.; Runser, A.; Bartenlian, H.; Nonat, A. M.; Charbonnière, L. J.; Klymchenko, A. S.; Hildebrandt, N.; Reisch, A. Lanthanide-Complex-Loaded Polymer

Nanoparticles for Background-Free Single-Particle and Live-Cell Imaging. *Chem. Mater.* **2019**, *31* (11), 4034–4041. https://doi.org/10.1021/acs.chemmater.9b00576.
(35) Tao, J.; Chow, S. F.; Zheng, Y. Application of Flash Nanoprecipitation to Fabricate Poorly Water-Soluble Drug Nanoparticles. *Acta Pharm. Sin. B* **2019**, *9* (1), 4–18. https://doi.org/10.1016/j.apsb.2018.11.001.
(36) Pino, P. del; Pelaz, B.; Zhang, Q.; Maffre, P.; Nienhaus, G. U.; Parak, W. J. Protein Corona Formation around Nanoparticles – from the Past to the Future. *Mater. Horiz.* **2014**, *1* (3), 301–313. https://doi.org/10.1039/C3MH00106G.
(37) Monopoli, M. P.; Åberg, C.; Salvati, A.; Dawson, K. A. Biomolecular Coronas Provide the Biological Identity of Nanosized Materials. *Nat. Nanotechnol.* **2012**, *7* (12), 779–786. https://doi.org/10.1038/nnano.2012.207.
(38) Ke, P. C.; Lin, S.; Parak, W. J.; Davis, T. P.; Caruso, F. A Decade of the Protein Corona. *ACS Nano* **2017**, *11* (12), 11773–11776. https://doi.org/10.1021/acsnano.7b08008.
(39) Gref, null; Lück, null; Quellec, null; Marchand, null; Dellacherie, null; Harnisch, null; Blunk, null; Müller, null. "Stealth" Corona-Core Nanoparticles Surface Modified by Polyethylene Glycol (PEG): Influences of the Corona (PEG Chain Length and Surface Density) and of the Core Composition on Phagocytic Uptake and Plasma Protein Adsorption. *Colloids Surf. B Biointerfaces* **2000**, *18* (3–4), 301–313.
(40) Moghimi, S. M.; Szebeni, J. Stealth Liposomes and Long Circulating Nanoparticles: Critical Issues in Pharmacokinetics, Opsonization and Protein-Binding Properties. *Prog. Lipid Res.* **2003**, *42* (6), 463–478. https://doi.org/10.1016/S0163-7827(03)00033-X.
(41) García, K. P.; Zarschler, K.; Barbaro, L.; Barreto, J. A.; O'Malley, W.; Spiccia, L.; Stephan, H.; Graham, B. Zwitterionic-Coated "Stealth" Nanoparticles for Biomedical Applications: Recent Advances in Countering Biomolecular Corona Formation and Uptake by the Mononuclear Phagocyte System. *Small* **2014**, *10* (13), 2516–2529. https://doi.org/10.1002/smll.201303540.
(42) Cheng, L.; Yang, K.; Chen, Q.; Liu, Z. Organic Stealth Nanoparticles for Highly Effective in Vivo Near-Infrared Photothermal Therapy of Cancer. *ACS Nano* **2012**, *6* (6), 5605–5613. https://doi.org/10.1021/nn301539m.
(43) Stolnik, S.; Heald, C. R.; Neal, J.; Garnett, M. C.; Davis, S. S.; Illum, L.; Purkis, S. C.; Barlow, R. J.; Gellert, P. R. Polylactide-Poly(Ethylene Glycol) Micellar-like Particles as Potential Drug Carriers: Production, Colloidal Properties and Biological Performance. *J. Drug Target.* **2001**, *9* (5), 361–378.
(44) Betancourt, T.; Byrne, J. D.; Sunaryo, N.; Crowder, S. W.; Kadapakkam, M.; Patel, S.; Casciato, S.; Brannon-Peppas, L. PEGylation Strategies for Active Targeting of PLA/PLGA Nanoparticles. *J. Biomed. Mater. Res. A* **2009**, *91A* (1), 263–276. https://doi.org/10.1002/jbm.a.32247.
(45) Jokerst, J. V.; Lobovkina, T.; Zare, R. N.; Gambhir, S. S. Nanoparticle PEGylation for Imaging and Therapy. *Nanomed.* **2011**, *6* (4), 715–728. https://doi.org/10.2217/nnm.11.19.
(46) Santander-Ortega, M. J.; Jódar-Reyes, A. B.; Csaba, N.; Bastos-González, D.; Ortega-Vinuesa, J. L. Colloidal Stability of Pluronic F68-Coated PLGA Nanoparticles: A Variety of Stabilisation Mechanisms. *J. Colloid Interface Sci.* **2006**, *302* (2), 522–529. https://doi.org/10.1016/j.jcis.2006.07.031.
(47) Fang, Z.; Chen, S.; Qin, J.; Chen, B.; Ni, G.; Chen, Z.; Zhou, J.; Li, Z.; Ning, Y.; Wu, C.; et al. Pluronic P85-Coated Poly(Butylcyanoacrylate) Nanoparticles Overcome Phenytoin Resistance in P-Glycoprotein Overexpressing Rats with Lithium-Pilocarpine-Induced Chronic Temporal Lobe Epilepsy. *Biomaterials* **2016**, *97*, 110–121. https://doi.org/10.1016/j.biomaterials.2016.04.021.

(48) Mehanny, M.; Hathout, R. M.; Geneidi, A. S.; Mansour, S. Studying the Effect of Physically-Adsorbed Coating Polymers on the Cytotoxic Activity of Optimized Bisdemethoxycurcumin Loaded-PLGA Nanoparticles. *J. Biomed. Mater. Res. A* **2017**, *105* (5), 1433–1445. https://doi.org/10.1002/jbm.a.36028.

(49) Moghimi, S. M.; Hunter, A. C. Poloxamers and Poloxamines in Nanoparticle Engineering and Experimental Medicine. *Trends Biotechnol.* **2000**, *18* (10), 412–420. https://doi.org/10.1016/S0167-7799(00)01485-2.

(50) Khalin, I.; Alyautdin, R.; Wong, T. W.; Gnanou, J.; Kocherga, G.; Kreuter, J. Brain-Derived Neurotrophic Factor Delivered to the Brain Using Poly (Lactide-Co-Glycolide) Nanoparticles Improves Neurological and Cognitive Outcome in Mice with Traumatic Brain Injury. *Drug Deliv.* **2016**, *23* (9), 3520–3528. https://doi.org/10.1080/10717544.2016.1199609.

(51) Kreuter, J. Drug Delivery to the Central Nervous System by Polymeric Nanoparticles: What Do We Know? *Adv. Drug Deliv. Rev.* **2014**, *71*, 2–14. https://doi.org/10.1016/j.addr.2013.08.008.

(52) Hatai, J.; Motiei, L.; Margulies, D. Analyzing Amyloid Beta Aggregates with a Combinatorial Fluorescent Molecular Sensor. *J. Am. Chem. Soc.* **2017**, *139* (6), 2136–2139. https://doi.org/10.1021/jacs.6b10809.

(53) *Topics in Fluorescence Spectroscopy: Principles*; Lakowicz, J. R., Ed.; Topics in Fluorescence Spectroscopy; Springer US, 2002.

(54) Ertürk, A.; Hellal, F.; Enes, J.; Bradke, F. Disorganized Microtubules Underlie the Formation of Retraction Bulbs and the Failure of Axonal Regeneration. *J. Neurosci.* **2007**, *27* (34), 9169–9180. https://doi.org/10.1523/JNEUROSCI.0612-07.2007.

(55) Liu Hanhan; Dienel Ari; Schöller Karsten; Schwarzmaier Susanne M.; Nehrkorn Kathrin; Plesnila Nikolaus; Terpolilli Nicole A. Microvasospasms After Experimental Subarachnoid Hemorrhage Do Not Depend on Endothelin A Receptors. *Stroke* **2018**, *49* (3), 693–699. https://doi.org/10.1161/STROKEAHA.117.020028.

(56) Frik, J.; Merl-Pham, J.; Plesnila, N.; Mattugini, N.; Kjell, J.; Kraska, J.; Gómez, R. M.; Hauck, S. M.; Sirko, S.; Götz, M. Cross-Talk between Monocyte Invasion and Astrocyte Proliferation Regulates Scarring in Brain Injury. *EMBO Rep.* **2018**, *19* (5), e45294. https://doi.org/10.15252/embr.201745294.

(57) Shibazaki, M.; Kawabata, Y.; Yokochi, T.; Nishida, A.; Takada, H.; Endo, Y. Complement-Dependent Accumulation and Degradation of Platelets in the Lung and Liver Induced by Injection of Lipopolysaccharides. *Infect. Immun.* **1999**, *67* (10), 5186–5191.

(58) Wang, L.; Tan, W. Multicolor FRET Silica Nanoparticles by Single Wavelength Excitation. *Nano Lett.* **2006**, *6* (1), 84–88. https://doi.org/10.1021/nl052105b.

(59) Hildebrandt, N.; Spillmann, C. M.; Algar, W. R.; Pons, T.; Stewart, M. H.; Oh, E.; Susumu, K.; Díaz, S. A.; Delehanty, J. B.; Medintz, I. L. Energy Transfer with Semiconductor Quantum Dot Bioconjugates: A Versatile Platform for Biosensing, Energy Harvesting, and Other Developing Applications. *Chem. Rev.* **2017**, *117* (2), 536–711. https://doi.org/10.1021/acs.chemrev.6b00030.

(60) Woll, D.; Braeken, E.; Deres, A.; De Schryver, F. C.; Uji-i, H.; Hofkens, J. Polymers and Single Molecule Fluorescence Spectroscopy, What Can We Learn? *Chem. Soc. Rev.* **2009**, *38*, 313–328. https://doi.org/10.1039/b704319h.

(61) Trofymchuk, K.; Reisch, A.; Shulov, I.; Mély, Y.; Klymchenko, A. S. Tuning the Color and Photostability of Perylene Diimides inside Polymer Nanoparticles: Towards Biodegradable Substitutes of Quantum Dots. *Nanoscale* **2014**, *6*, 12934–12942. https://doi.org/10.1039/C4NR03718A.

(62) Elson, E. L. Fluorescence Correlation Spectroscopy: Past, Present, Future. *Biophys. J.* **2011**, *101* (12), 2855–2870. https://doi.org/10.1016/j.bpj.2011.11.012.
(63) Bazile, D.; Prud'homme, C.; Bassoullet, M.; Marlard, M.; Spenlehauer, G.; Veillard, M. Stealth Me. PEG-PLA Nanoparticles Avoid Uptake by the Mononuclear Phagocytes System. *J. Pharm. Sci.* **1995**, *84* (4), 493–498. https://doi.org/10.1002/jps.2600840420.
(64) Xu, Q.; Boylan, N. J.; Cai, S.; Miao, B.; Patel, H.; Hanes, J. Scalable Method to Produce Biodegradable Nanoparticles That Rapidly Penetrate Human Mucus. *J. Control. Release Off. J. Control. Release Soc.* **2013**, *170* (2), 279–286. https://doi.org/10.1016/j.jconrel.2013.05.035.
(65) Vonarbourg, A.; Passirani, C.; Saulnier, P.; Benoit, J.-P. Parameters Influencing the Stealthiness of Colloidal Drug Delivery Systems. *Biomaterials* **2006**, *27* (24), 4356–4373. https://doi.org/10.1016/j.biomaterials.2006.03.039.
(66) Röcker, C.; Pötzl, M.; Zhang, F.; Parak, W. J.; Nienhaus, G. U. A Quantitative Fluorescence Study of Protein Monolayer Formation on Colloidal Nanoparticles. *Nat. Nanotechnol.* **2009**, *4* (9), 577–580. https://doi.org/10.1038/nnano.2009.195.
(67) Jeon, S. I.; Lee, J. H.; Andrade, J. D.; De Gennes, P. G. Protein—surface Interactions in the Presence of Polyethylene Oxide: I. Simplified Theory. *J. Colloid Interface Sci.* **1991**, *142* (1), 149–158. https://doi.org/10.1016/0021-9797(91)90043-8.
(68) Albota, M. A.; Xu, C.; Webb, W. W. Two-Photon Fluorescence Excitation Cross Sections of Biomolecular Probes from 690 to 960 Nm. *Appl. Opt.* **1998**, *37* (31), 7352–7356. https://doi.org/10.1364/ao.37.007352.
(69) Kucherak, O. A.; Oncul, S.; Darwich, Z.; Yushchenko, D. A.; Arntz, Y.; Didier, P.; Mély, Y.; Klymchenko, A. S. Switchable Nile Red-Based Probe for Cholesterol and Lipid Order at the Outer Leaflet of Biomembranes. *J. Am. Chem. Soc.* **2010**, *132* (13), 4907–4916. https://doi.org/10.1021/ja100351w.
(70) Moore, T. L.; Rodriguez-Lorenzo, L.; Hirsch, V.; Balog, S.; Urban, D.; Jud, C.; Rothen-Rutishauser, B.; Lattuada, M.; Petri-Fink, A. Nanoparticle Colloidal Stability in Cell Culture Media and Impact on Cellular Interactions. *Chem. Soc. Rev.* **2015**, *44* (17), 6287–6305. https://doi.org/10.1039/c4cs00487f.
(71) Dante, S.; Petrelli, A.; Petrini, E. M.; Marotta, R.; Maccione, A.; Alabastri, A.; Quarta, A.; De Donato, F.; Ravasenga, T.; Sathya, A.; et al. Selective Targeting of Neurons with Inorganic Nanoparticles: Revealing the Crucial Role of Nanoparticle Surface Charge. *ACS Nano* **2017**, *11* (7), 6630–6640. https://doi.org/10.1021/acsnano.7b00397.
(72) Bowen, S.; Ateh, D. D.; Deinhardt, K.; Bird, M. M.; Price, K. M.; Baker, C. S.; Robson, J. C.; Swash, M.; Shamsuddin, W.; Kawar, S.; et al. The Phagocytic Capacity of Neurones. *Eur. J. Neurosci.* **2007**, *25* (10), 2947–2955. https://doi.org/10.1111/j.1460-9568.2007.05554.x.
(73) Li, K.; Zhu, Z.; Cai, P.; Liu, R.; Tomczak, N.; Ding, D.; Liu, J.; Qin, W.; Zhao, Z.; Hu, Y.; et al. Organic Dots with Aggregation-Induced Emission (AIE Dots) Characteristics for Dual-Color Cell Tracing. *Chem. Mater.* **2013**, *25* (21), 4181–4187. https://doi.org/10.1021/cm401709d.
(74) Danhier, F. To Exploit the Tumor Microenvironment: Since the EPR Effect Fails in the Clinic, What Is the Future of Nanomedicine? *J. Control. Release Off. J. Control. Release Soc.* **2016**, *244* (Pt A), 108–121. https://doi.org/10.1016/j.jconrel.2016.11.015.
(75) Simpson, B. W.; Trent, M. S. Pushing the Envelope: LPS Modifications and Their Consequences. *Nat. Rev. Microbiol.* **2019**, *17* (7), 403–416. https://doi.org/10.1038/s41579-019-0201-x.
(76) Nishioku, T.; Dohgu, S.; Takata, F.; Eto, T.; Ishikawa, N.; Kodama, K. B.; Nakagawa, S.; Yamauchi, A.; Kataoka, Y. Detachment of Brain Pericytes from the Basal Lamina Is Involved in Disruption of the Blood-Brain Barrier Caused by Lipopolysaccharide-

Induced Sepsis in Mice. *Cell. Mol. Neurobiol.* **2009**, *29* (3), 309–316. https://doi.org/10.1007/s10571-008-9322-x.

(77) Jangula, A.; Murphy, E. J. Lipopolysaccharide-Induced Blood Brain Barrier Permeability Is Enhanced by Alpha-Synuclein Expression. *Neurosci. Lett.* **2013**, *551*, 23–27. https://doi.org/10.1016/j.neulet.2013.06.058.

(78) Banks, W. A.; Gray, A. M.; Erickson, M. A.; Salameh, T. S.; Damodarasamy, M.; Sheibani, N.; Meabon, J. S.; Wing, E. E.; Morofuji, Y.; Cook, D. G.; et al. Lipopolysaccharide-Induced Blood-Brain Barrier Disruption: Roles of Cyclooxygenase, Oxidative Stress, Neuroinflammation, and Elements of the Neurovascular Unit. *J. Neuroinflammation* **2015**, *12*, 223. https://doi.org/10.1186/s12974-015-0434-1.

(79) Li, H.; Wang, P.; Huang, F.; Jin, J.; Wu, H.; Zhang, B.; Wang, Z.; Shi, H.; Wu, X. Astragaloside IV Protects Blood-Brain Barrier Integrity from LPS-Induced Disruption via Activating Nrf2 Antioxidant Signaling Pathway in Mice. *Toxicol. Appl. Pharmacol.* **2018**, *340*, 58–66. https://doi.org/10.1016/j.taap.2017.12.019.

(80) Kuperberg, S. J.; Wadgaonkar, R. Sepsis-Associated Encephalopathy: The Blood-Brain Barrier and the Sphingolipid Rheostat. *Front. Immunol.* **2017**, *8*, 597. https://doi.org/10.3389/fimmu.2017.00597.

(81) Bharadwaj, V. N.; Nguyen, D. T.; Kodibagkar, V. D.; Stabenfeldt, S. E. Nanoparticle-Based Therapeutics for Brain Injury. *Adv. Healthc. Mater.* **2019**, 1700668. https://doi.org/10.1002/adhm.201700668@10.1002/(ISSN)2192-2659.Nanotherapeutics.

(82) Ruozi, B.; Belletti, D.; Sharma, H. S.; Sharma, A.; Muresanu, D. F.; Mössler, H.; Forni, F.; Vandelli, M. A.; Tosi, G. PLGA Nanoparticles Loaded Cerebrolysin: Studies on Their Preparation and Investigation of the Effect of Storage and Serum Stability with Reference to Traumatic Brain Injury. *Mol. Neurobiol.* **2015**, *52* (2), 899–912. https://doi.org/10.1007/s12035-015-9235-x.